EXPERIMENTAL AND NUMERICAL INVESTIGATION OF MASS TRANSFER IN MICROREACTORS

by

WEI HAN

Presented to the Faculty of the Graduate School of
The University of Texas at Arlington in Partial Fulfillment
of the Requirements
for the Degree of

DOCTOR OF PHILOSOPHY

THE UNIVERSITY OF TEXAS AT ARLINGTON

May 2012

ACKNOWLEDGEMENTS

I would like to express my sincere gratitude to my supervising professor Dr. Brian H. Dennis for his continuous support throughout my Ph.D study and research, for his patience, enthusiasm, motivation, and immense knowledge. His technical and editorial advice was essential to the completion of this dissertation. His engineering intuition has made him a great professor and researcher. His mentorship was paramount in providing a well rounded experience in my academic career, and it will also consistently have a positive influence on my long-term professional career.

I would also like to acknowledge Dr. Kent Lawrence, Dr. Bo Ping Wang, Dr. Ratan Kumar, and Dr. Seiichi Nomura for kindly accepting for serving on my Ph.D committee. Their advice and assistance are greatly appreciated.

I also would like to thank my CFD lab colleagues and CREST lab colleagues Takahiro Sonoda, Rajeev Kumar, Weiya Jin, Dolly Pan Richards, Chinmay Adhvaryu, Ai Ueno, Rachaneewan Charoenwat, Travis Carrigan, Deval Pandya, Xiao Zhang, Harsh Shah, Kamal Chauhan, Olivia Choi, and Wilaiwan Chanmanee for all their friendship and cooperation.

I would like to thank my parents and my sister, for their encouragement and patience throughout my education. I am extremely grateful to my uncle Zhen Xue Han and his family for their support and encouragement throughout my graduate

study.

April 20, 2012

ABSTRACT

EXPERIMENTAL AND NUMERICAL INVESTIGATION
OF MASS TRANSFER IN MICROREACTORS

Wei Han, Ph.D.

The University of Texas at Arlington, 2012

Supervising Professor: Brian H. Dennis

In this work, two types of microreactors for reactions have been studied, which were involving multiple fluid phases: liquid-liquid (immiscible liquids) phase and gas-liquid phase. Investigation of mass transfer within reacting flows in microreactors has been carried out in these two multiphase systems. For the liquid-liquid phase, a microfluidic system was designed and fabricated to generate a slug flow pattern of immiscible liquids. This system was used to demonstrate the effect of the flow pattern on mass transfer and the effect on chemical reaction rate for a simple acid-base reaction. The reaction progression was tracked by measuring the pH along the length of the microchannel. A detailed mathematical model included mass transfer and reaction kinetics was constructed and solved numerically using computational fluid dynamics software. The kinetic rate constant was determined from the experiment data using an optimization algorithm. A good match between experimental results and numerical model was obtained. For the gas-liquid studies, a microfluidic device that consists of a microporous polymer membrane and microchannels has been designed and fabricated. The device was used to test mass transfer from gas to liquid

water phase for both oxygen and carbon dioxide. The correlated Sherwood number was presented for different average flow velocity. The impact of channel geometry and residence time on reaction completeness was also measured for carbon dioxide reacting with an aqueous alkaline solution. The experiment results were compared with a numerical model solved with computational fluid dynamics software. Potential application of the developed devices and their results include compact units for carbon dioxide capture from gas mixtures and portable blood oxygenators.

TABLE OF CONTENTS

LIST OF FIGURES

LIST OF TABLES

CHAPTER 1

INTRODUCTION AND LITERATURE REVIEW

1.1 Introduction

Microprocess technology and microsystem technology both involve interdisciplinary engineering, physical science branches, chemistry and biology. In most cases, the management techniques and economics influence are also involved. They both are used in various applications, such as food processing, energy conversion, and mass and heat transfer enhancement, chemical synthesis and so on [1]. In this study, chemical process engineering will be the focus and the benefit on mass transfer intensification will be investigated. The entire microprocess and microsystem not only involve the experimental design, physical processing, chemical reaction and computer calculation, but also involve the material selection, apparatus design, and manufacturing.

Generally, microtechnology is defined as the technology with a dimension of one millimeter or less. It usually involves a microstructure which is the major component in the microprocess and microsystem. Normally, microstructures include microchannels, microtubes, micropumps, and microreactors. There are several restrictions to the micro scale device, including the manufacture, assembling, testing and visualization. Along with development of MEMS technique, the manufacturing technique provides more possibilities to meet the miniaturization requirement. The internal microstructure can be arranged in parallel and the entire micro-unit can be stacked up externally to satisfy the required input and output. Microstructures can also be used to build up portable devices while achieving the required amount of throughput.

Microprocess and microsystem are widely used in mass and heat transfer intensification. They both include the substances injection, mixing, separation and purification. Mixing is a fundamental and important element in mass transport. In the physical process, the chemical reaction may or may not be involved. The mixing unit, which consists of apparatus and mixing element, such as microchannels, microtubes, micropores, and microplates, are also important mixing components. In this study, mass transfer with chemical reaction is investigated.

1.2 General Literature Review of Microreactors

A microreactor is a type of novel reactor which allows chemical reactions to take place inside a smaller structure, usually with a dimension of a micron or less. Microreactors have also been defined as microstructures for SMART reactors: precision performance in industrial production [2]. Microreactors allows to highly integrate multiple functions on one device. Microreactors are not only capable to form a single fully functional device but also are flexible to be a partial component in a system. It can be applied to laboratory use as well as the industrial use. A great number of microreactors have been developed and used in various applications, such as chemical engineering, food processing, and bioengineering. They have the potential to enable faster mass and heat transfer and result in desired output. The production capacity can be scaled up by stacking up microreactor elements. Microreactors also help to lower the cost of material, transportation and energy input, while being more flexible to meet market demands. Microreactors usually involve mass, momentum, and energy transport during the entire process. The corresponding driving forces are the gradients in concentration, velocity, and temperature [3].

The main components of microreactors are microchannels, microtubes, microplates, and microbeds, which are all made out of regular geometry, such as rect-

angles, squares, and circles. These regular shapes are chosen to reduce the difficulties of fabrication and ensure precise fabrication for easy operation control. Typical materials used to construct microreactors are different types of polymers, silicon, glass, silicon compounds, and stainless steel. Usually, the surface property of these materials can be modified with functionalized coating by a chemical treatment. Normally, there are two common surface properties, that play important roles in microprocess, are hydrophobic and hydrophilic. There are several microfabrication techniques available for microreactor fabrication, such as micromaching, laser cutting, wet and dry chemical etching, soft lithography, and electroforming [1].

Microreactors show promising potential for mass intensification in a continuous process, especially for the mixing of immiscible fluids.Most microreactors are used for mixing and separation of liquid-liquid phases, liquid-gas phases or gas-gas phases. Within the critical dimension of the microreactor, the ratio of the interfacial area between different phases can be increased [3]. This significantly increases conversion rate and reduces reaction time; it can also help reduce the amount of catalyst. Due to the characteristic dimension, the flowing element can be cooled down and heated up rapidly, which reduce high pressure and high temperature safety concerns during operation.

For different types of microreactors, the additional surface effects need to be included in the multiphase flow, such as emulsification, taylor flow, and droplets generation [4],[5],[6]. The ratio of surface to volume is larger in a microstructure. This benefits mass and heat transfer for pure diffusion and convection-diffusion transport. For pure diffusion, the diffusion length can be shortened due to the small length scale. Regarding convective effects, the curved features inside the microchannel or microtube cause secondary flow which help to enhance mixing efficiency by inducing chaotic flow

[7]. For a microplate or microbed, micropillars are introduced and attached to the bottom surface to increase the contact surface [8],[9].

Most applications involved gas-liquid phase are gas exchanger systems and micro scale gas absorption systems. A great number of gas exchange devices have been designed and evaluated through experimental and numerical methods; however, the fabrication of the nanoporous membrane takes a lot of time using nanotechnology. The silicon nanoporous membrane is not very durable for long term use, which potentially increases the cost of gas exchange [10]. Throughout most of the studies, hollow fiber membranes were the major component in gas-liquid contact system, which are used to test and construct the gas exchange device in a smaller scale; however, they have issues dealing with higher flow rate due to structural limitations [11].

Results including theoretical and numerical analysis were presented while studying mass transport in microstructures. The analytical solution of mass transfer in a hollow tube membrane with heterogeneous chemical reaction has been done by Loney [12]. Computational fluid dynamics (CFD) techniques can also be used to understand microprocessing technology and predict transport phenomena in a micro scale. CFD techniques were initially developed and used for validation of aircraft design. For the past few decades, it has been used in different types of microfluidic analysis. Numerous simulation cases have conducted for different flow type in microchannels, microtubes, and microducts, in order to investigate the mass transfer and heat transfer in multiphase systems [13],[14],[15]. The combination of experimental and numerical studies efficiently help to evaluate microreactor performance [16].

1.3 Objectives

In this study, two major types of microreactors will be evaluated experimentally and numerically. The first type of microreactor is a capillary reactor with slug flow

generation, which has a large mixing potential for multiphase and immiscible fluids [17]. The relation between flow rate, slug size, and mixing efficiency will be investigated through experimental and computational studies. Another type microreactor involves gas phase and liquid phase, separately. Two different gas-liquid membrane microreactors will be used to carry out the gas transport experiment. One membrane microreactor is designed to test oxygen (O_2) and carbon dioxide CO_2 transport through microporous membrane and to exam convective effect on gas transport in a reacting flow by calculating the Sherwood number. Based on the factors of governing gas exchange efficiency in membrane, the large membrane surface area, the good diffusion characteristics, and the good membrane, the membrane microreactor will be designed, built, and tested. The function of this microreactor is to demonstrate the effect of liquid flow rate on O_2 and CO_2 transport through the microporous membrane, which has the potential to be used for the oxygenator.

Another microreactor will be built to evaluate gas absorption through a microporous membrane in a reacting flow involved gas phase and liquid phase, meanwhile, detailed reaction kinetics will be presented for investigate the reaction rate and mass transfer rate. Two different microchannel pattern will be designed and tested with same fixture; one is a straight microchannel and the other one is a meandering microchannel. The effect of solvent concentration, solvent flow rate, gas flow rate, and microchannel pattern on the gas transport will be presented. In addition, computational models are established for two different microchannel designs. Effect of different solvent flow rates on gas transport for a straight microchannel is predicted. Mass fraction distribution of each species are obtained by implementing detailed reaction kinetics to the computational models.

CHAPTER 2

EXPERIMENTAL AND NUMERICAL INVESTIGATION OF MASS TRANSFER WITH LIQUID-LIQUID TWO PHASE SLUG FLOW IN A MICROCHANNEL

2.1 Background

The multiphase flow involving two immiscible liquids in a micromixer was investigated experimentally and numerically. The mass transfer characteristics of this flow pattern are of primary interest in this study. A simple neutralization titration reaction was chosen as the basis. The liquid-liquid two phase slug flow was formed during the mixing. The mixing was quantified for different volume flow rates of the reactants. To simplify the computational procedure, instead of applying different volume flow rate, the wall was moved with different average slug flow velocity. It was shown that the residence time required for reaction completeness was dominated by the average flow velocity for this type of micromixer. Furthermore, a parametric two-dimensional model was implemented with COMSOL Multiphysics to investigate mixing phenomenon within the slugs. The COMSOL model allows for rapid analysis of different flow rates. Based the of experimental data and numerical simulation, the kinetic rate constant k was evaluated using an optimization algorithm.

Slug flow is a type of two-phase flow pattern formed either inside capillary or microchannel. There are two major types of slug flow: gas-liquid and liquid-liquid two phase flow. Slug flow has been widely used in biomedical and engineering applications, because of the intensification of heat and mass transfer with the large surface-to-volume ratio and the internal circulation within slugs in micro scale.

Burns and Ramshaw [18] presented the intensification of mass transfer with slug flow in a capillary channel with a simple titration reaction. The details of slug generation, slug size, and pressure drop were described by Kashid and Agar [19] with a capillary microreactor. The quantitative study of the mass transfer with two immiscible fluids in a T-shaped microchannel system has been investigated by Zhao et al. [17]. A great number of studies have proved that the slug flow plays an important role in the process of mass transfer in microsystem.

With the development and application of MEMS technology, the micro scale reactor has become the new topic in chemical engineering and biotechnology fields. It has been demonstrated that microreactor technology provides potential benefits to processing technology, especially in chemical reaction engineering [20]. The benefits of the microreactor are not only a decrease in the mixing time but also work to enhance the heat and mass transfer [21]. A transesterification reaction implemented with a capillary microreactor for catalyzed synthesis of biodiesel shows the significant effect of a micro scale reactor in chemical processing [22]. For those applications, the mixing of two phases with a chemical reaction is of interest and can increase the mass transfer efficiency between two insoluble phases [23]. Zhao et al. [24] experimentally compared parallel flow and slug flow in a rectangular microchannel with different Weber number based on the mass transfer between deionized water and kerosene. A quantitative study of discrete drop mixing in a microchannel demonstrated three types of transport phenomena: diffusion-oriented, dispersion-oriented, and convection-oriented, according to different P*é*clet number [25]. Soleymani et al. [16] computationally investigated the mixing phenomena in a T-type microchannel with a low Reynolds number (Re<250), as well as, presented results demonstrating significant mixing efficiency due to the formation of vortices in the flow field.

CFD describes the flow field by solving a set of conservation equations. The concentration of the chemical species and other scalar variables will be also included in the solution of the algebraic equations. The numerical analysis using CFD was applied to study the mass transfer with liquid-liquid slug flow [14],[15],[26],[27]. From the strength of the numerical simulations, more micro scale transport phenomena will be observed than in the experimental studies.

The global mass transfer characteristics in microsystems have been evaluated. However, the details of mass transfer phenomena for liquid-liquid slug flow with chemical reaction kinetics have not been well understood, such as the influence from reaction rate and the specific diffusion coefficient within two different phases, as well as the effect of aspect ratio on the mixing efficiency.

2.2 Experiment

In the present work, the numerical analysis will be performed using COMSOL Multiphsics which is based on Finite Element Method (FEM). To investigate the mixing efficiency and mixing phenomenon inside slugs, the residence time under different flow conditions will be studied. The residence time required for 99% conversion of KOH will be quantified with different average flow velocities. Moreover, the effect of average flow velocity with a fixed size radius will also be presented and the rate constant will be evaluated.

A simple neutralization titration reaction was used as the basis for the study because the reaction takes place without any additional condition. This neutralization titration reaction can be carried out under room temperature (20°C) and without a catalyst; it also has advantage that it is a simple and safe reaction without any toxic results produced. Furthermore, it is easy to get the measurements by observing the change in color due to the conventional pH indication in the reactants within the

reaction. Color change resulted by pH value change helps to distinguish the two phases along with the slug flow. This technique helps to construct a computational model for comparison due to the simple chemical kinetics.

2.2.1 Solution Preparation

Kerosene with acetic acid and potassium hydroxide (KOH) were selected as the reactants for testing the mass transfer in the mcirochannel. Acetic acid (AA) (ACROS) was added into the pure kerosene (ACROS Organics) to make 650 mol/m^3 solutions, which was considered as the organic phase. The 250 mol/m^3 of KOH aqueous solution was made with potassium hydroxide solid pellets (Mallinckrodt Chemicals) and regular water. It was selected as the base reactant. Hence, the phenol red pH indicator (Ricca Chemical Cop.) was added into potassium hydroxide solution. This alkaline aqueous solution was considered as the aqueous phase. The 5ml plastic syringes (Luer-Lok^{TM} Tip) with Polytetrafluoroethylene (PTFE) capillary tube (Upchurch Scientific) were used for injecting the feed liquids.

2.2.2 Experiment Set-up

The experiment was performed using a Y-shaped microchannel as the prototype for the microreactor which was made of High-density polyethylene (HDPE). This type of material can prevent water, water containing solutions, oil and oil containing solutions from adhering to the wall of the microchannel. In another words, the hydrophobic surface of HDPE has the same characteristics as PTFE for decreasing the transport path between two adjacent slugs, making it capable of chemically resistant.

The Y-shaped mcrochannel was cut out on a HDPE film using micromilling processing and the schematic feature is shown in Fig. 2.1. The microchannel has a square cross section with dimension of 500μm$\times$500μm. The two inlet guide ducts with

same dimension as the microchannel lie at an angle of 60 degrees and the transport region has a length of 130mm. The microchannel was covered with a thin HDPE film with a thickness of 254μm to make the properties of the fluid consistent across the contact surface. The thin HDPE film was also transparent so that it makes the fluids visible during the experiment. The microchannel with the cover was supported by the polycarbonate with a thickness of 9.525 mm on the top and bottom. The silicone tubes connected with PTFE capillary tubes have an inner diameter of 1mm and were used as feed ducts and the product outlet in Fig. 2.2.

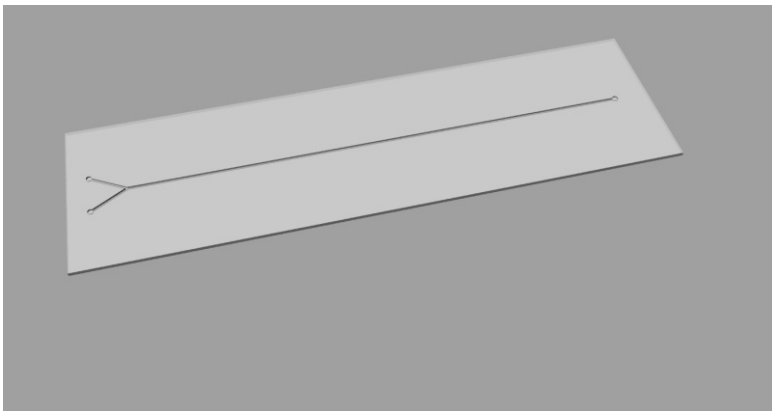

Figure 2.1. Schematic feature of Y-shaped microchannel.

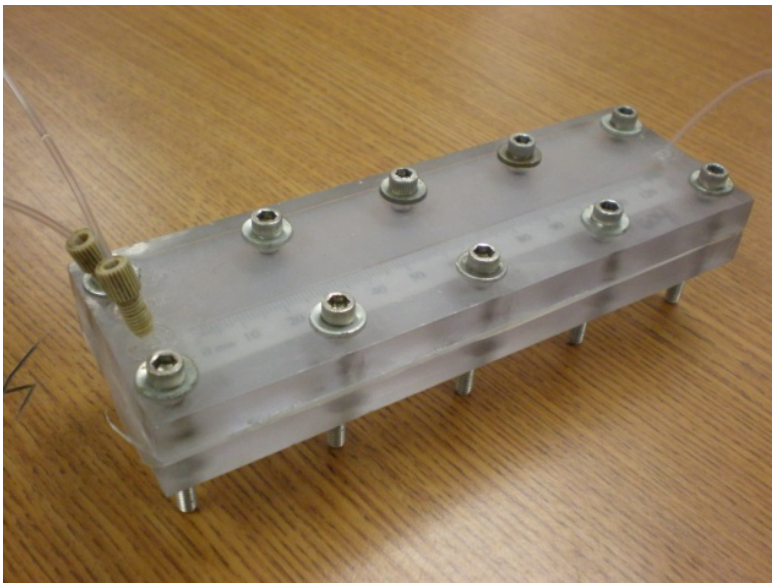

Figure 2.2. Actual feature of Y-shaped microreactor.

2.2.3 Methods and Results

The simple neutralization reaction mechanism involved in this study is shown in Eqn. 2.1.

$$CH_3COOH + KOH \xrightarrow{k} CH_3COOK + H_2O \tag{2.1}$$

Two immiscible liquids were driven into the Y-shaped microchannel by a micropump through syringes. The experiment schematic is illustrated in Fig. 2.3. The flow ratio was fixed at 1:1 because the two syringes were pushed with same flow rate by the micropump. The flow velocity range is 0.0028m/s−0.0156m/s. Two feed fluids were confluent at the beginning of the transport region. One liquid flowed through the Y-junction, while the other liquid interrupted the flow and resulted in an alternating flow structure.

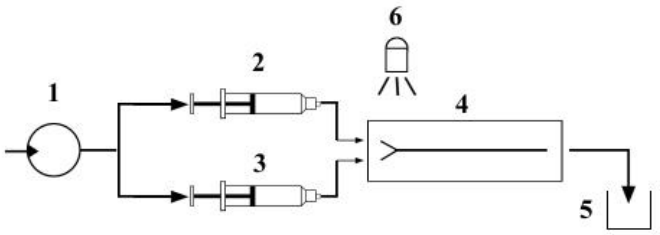

Figure 2.3. Schematic diagram of experiment with (1) micropump, (2) aqueous phase syringe, (3) organic phase syringe, (4) Y-shaped microchannel, (5) products, (6) digital microscopy.

In the transport region, slug flow was formed due to the same low flow rate, low Reynolds number, size of the microchannel, and the surface property of the contacting area. The two immiscible liquids were both continuous phases during the mass transfer process. To analyze the transport performance, measurements of color change distance along the microchannel were taken with the digital microscopy (AM 311S, DinoLite, AnMo Electronics Cop.). It is easy to distinguish two phases because the aqueous phase was mixed with pH indicator which appears as a red color in a basic aqueous solution. It was found that the reaction took place between two adjacent phases and mainly in the aqueous phase. The mass transfer zone starts from the meeting point in the Y-junction and ends at the outlet. The experiment ran as slow as possible to avoid the mass transfer in the outlet conduit. At each flow rate, there were at least five measurements recorded.

The solubility of potassium hydroxide (KOH) in the organic phase is much weaker compared with the solubility of the acetic acid in the aqueous phase because acetic acid can completely dissolve in the aqueous phase. The acetic acid diffused across the interface and reacted with potassium hydroxide. The color change in the

pH indicator illustrated the molecules of acetic acid diffused into the aqueous slug and reacted with the potassium hydroxide. The reaction resulted in a color change (red to yellow) in the aqueous phase Fig. 2.4.

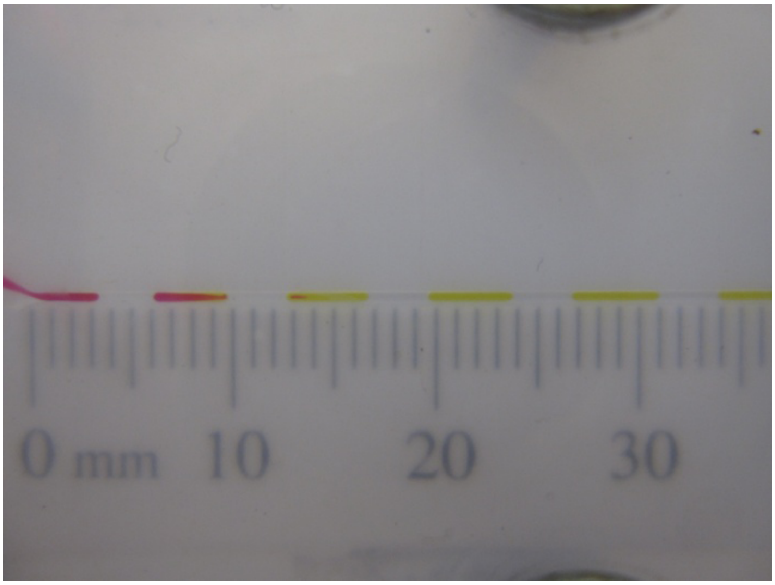

Figure 2.4. Slug generation and completion of reaction at flow rate 0.5ml/hr; the aqueous phase is in red and organic phase is colorless.

The distance required to complete the color change within the aqueous slug was measured while experiment was running. The data was recorded every five minutes. The average color change distance is proportional to the flow rate as shown in Fig. 2.5. The figure also goes to show that the color change distance is increasing as the flow rate is increased. It is also worth noting that slug length becomes shorter as flow rate increases. As shown in Fig. 2.6, the lengths of the two slugs are not exactly equal to each other and the difference is decreasing as flow rate increases.

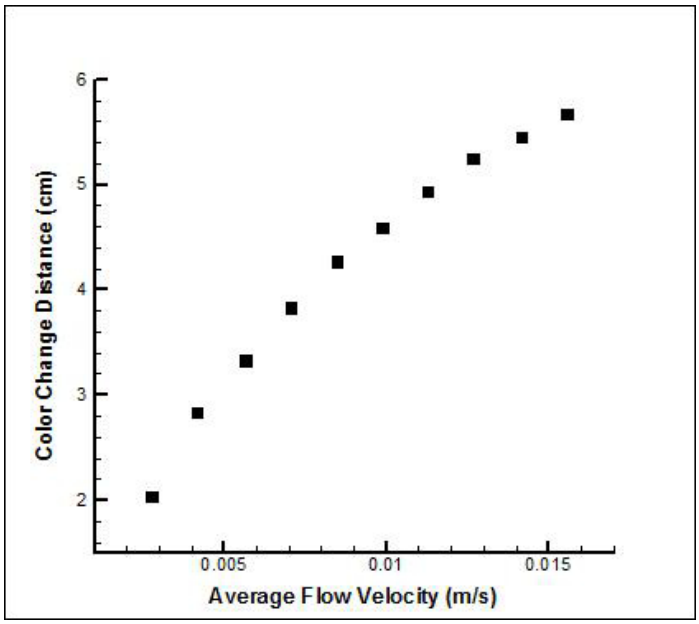

Figure 2.5. Average pH color change distance along microchannel at different flow rate.

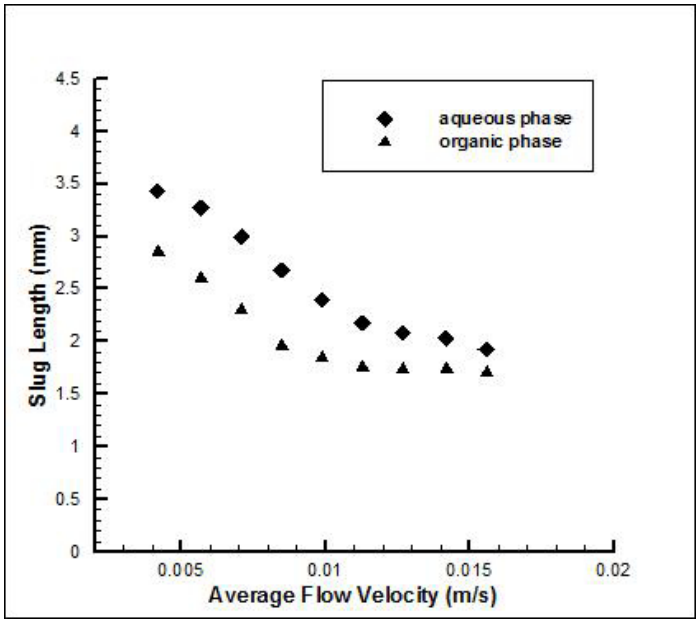

Figure 2.6. Average slug length along microchannel at different flow rate.

Generally, there are two different situations encountered during slug generation. One case is that one phase is surrounded by the film which is formed by another phase. The other case is that the slugs are connected end and end to are attached to the interior wall of channel. In the first case, the available interfacial area for mass transfer is much larger than the interfacial area in the second case.

2.3 Computational Model

From experimental abservation and images taken by microscopy, it was found that no film surrounding the slugs. Based on the experimental observation, we assume that only the ends of the slugs were involved in the mass transfer. Therefore, under the previous assumption, the computational domain can be defined as the following seen in Fig. 2.7.

Figure 2.7. Schematic representation of the computational domain; 1 represents aqueous phase and 2 represents organic phase.

To investigate the flow behaviour inside the microchannel, a two dimensional slice of the microchannel was to be considered due to the axisymmetric nature of the flow. The computational domain consisted of two adjacent rectangular units which represent the two immiscible phases, one is an organic phase and the other one is an aqueous phase, which is due to the characteristic of slug flow formation.

The Largrangian reference frame is used for the simulation. A pair of slugs were selected to be studied. Rather than computing the whole series of alternating slugs, studying a single pair of slugs can reduce the computational effort. The width and the length of the rectangle represent the radius and the length of each phase respectively.

In this work, the computational scheme assumed that the slugs were held stationary while the wall of the microchannel was moving with a constant velocity equal to the average flow velocity. The different chemical species had to be defined, identified by density and viscosity.

2.3.1 Governing Equations

For fluid flow, the Navier-Stokes equations (Eqn. 2.2 and Eqn. 2.3) were solved numerically using the finite element method in COMSOL with Matlab 3.5. Both phases were assumed to be incompressible with Newtonian behavior. The shape and volume of the slugs remained the same during the mass transfer and chemical reaction. The flow was laminar due to the small Reynolds number. The velocity field is solved under steady state. The density and dynamic viscosity, ρ and μ respectively are constants for both phases. The pressure p can be solved from the following equations, which are continuity equation Eqn. 2.2 and conservation of momentum equation Eqn. 2.3.

$$\nabla \cdot \vec{u} = 0 \tag{2.2}$$

$$\rho(\vec{u} \cdot \nabla)\vec{u} = -\nabla p + \mu \nabla^2 \cdot \vec{u} \tag{2.3}$$

The mass transfer between two phases is governed by the general convection-diffusion equation Eqn. 2.4

$$\frac{\partial C_{mn}}{\partial t} + \vec{u} \cdot \nabla C_{mn} = \nabla \cdot (D_{mn} \nabla C_{mn}) \pm R_{ij} \tag{2.4}$$

Where, C_{mn} is the concentration of chemical m in domain n. Index m=2 represents two chemicals which are acetic acid (AA) and KOH, respectively, and index n=2 represents two domains which are the base phase and the acid phase. D_{mn} is the diffusion coefficient of solute p in solvent n, which was calculated from Wilke-Chang correlation Eqn. 2.6 [28]. R_{ij} is a source term which represents the contribution of the chemical reaction. Indices i and j represent the two reactants. The reaction is a second order irreversible reaction. The reaction rate R_{ij} can be expressed as follow Eqn. 2.5.

$$R_{ij} = kC_iC_j \tag{2.5}$$

where, i and j represent the two reactants, AA and KOH, and k is the kinetic rate constant.

$$D_{mn} = 7.4 \times 10^{-8} \frac{T\sqrt{\varphi_n M_n}}{\mu_n V_m^{0.6}} \tag{2.6}$$

In Eqn. 2.6 [28], D_{mn} represents the diffusion coefficient of solute m in solvent n, T is the temperature in Kelvin, and φ_n is the association parameter which has a value of 2.6 for aqueous phase and value of 1 for other unassociated solvents such as organic phases; μ_n is the dynamic viscosity of the solvent; M_n is the molecular weight of solute and solvent; V_m is the molar volume of the solute, which can be obtained by Le Bas method [29], respectively.

2.3.2 Simulation Conditions

To solve the convection-diffusion equation numerically, the computations were conducted in two stages. First, the velocity profile was obtained by numerically solving the continuity and momentum equations under steady state conditions. The concentration distributions for the two domains were obtained by solving the convection-diffusion equation with a velocity profile implementation.

The boundary condition at the moving wall was assigned with the average velocity of the fluids. A condition of equal stress, $\mu_1 \partial u/\partial r = \mu_2 \partial u/\partial r$, was applied on the interface of the two domains. Furthermore, r=0 was assigned to the central axis to ensure the axisymmetric nature. With regard to the mass transfer, the flux continuity at the interface was satisfied with the following relation: $D_{m1}\partial C_{m1}/\partial n_1 = D_{m2}\partial C_{m2}/\partial n_2$. On the moving wall, $\partial C_{mn}/\partial n$=0 was assigned, which indicated that there is no mass flux through the wall, and nn is the normal vector to the interface. The periodic boundary was also implemented on the connected interface and r=0 was imposed to the central axis. Additionally, the concentration of two species were initialized at t=0 for domain 1 and domain 2 (base phase and acid phase), which were 250mol/m^3 and 650mol/m^3 respectively. A uniform structured mesh with 3,000 elements was used, seen in Fig. 2.8. In this figure, two axes are independent.

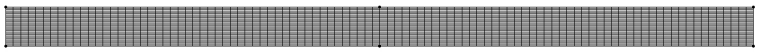

Figure 2.8. Uniform structured mesh; 3,000 elements.

2.3.3 Mesh Dependency Study

A structured mesh topology was chosen to discretize the computational domain. For this study, two different meshes were investigated. A uniform structured mesh was studied first. The individual mesh cell has an aspect ratio of 9.6 with a total number of 3,000 cells. With this type of mesh, it was not easy to capture the velocity gradient. Therefore, another structured mesh was constructed. Instead of using a uniform mesh, the mesh was clustered at the interface and close to the wall to capture the interface phenomena and the velocity gradient. Different cell sizes and mesh refinement levels were evaluated until better convergence was achieved. The mesh shown below in Fig. 2.9 was the final mesh which contains 25,600 cells. In this figure, two axes are independent.

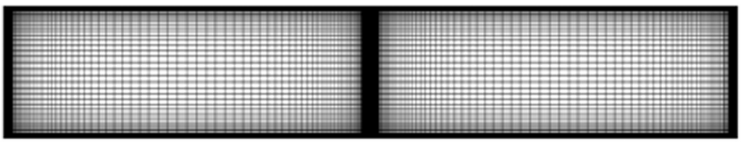

Figure 2.9. Refined mesh, 25,600 elements.

2.3.4 Mass Transfer Model and Results

To solve the governing equations numerically, the equations were discretized by using the backward differentiation formulas (BDF) method with a small time step size. As described earlier, the computational approach was based on solving the N-S equations to obtain the velocity field which was then used to solve the convection-diffusion equation. The flow field was solved in a steady state due to the small Reynolds number in two regions. The streamline plot in Fig. 2.10 clearly shows that

internal circulations formed inside both slugs. The solved flow field of two phases is shown in Fig. 2.11. In these two plots, two axes are independent for better visualization.

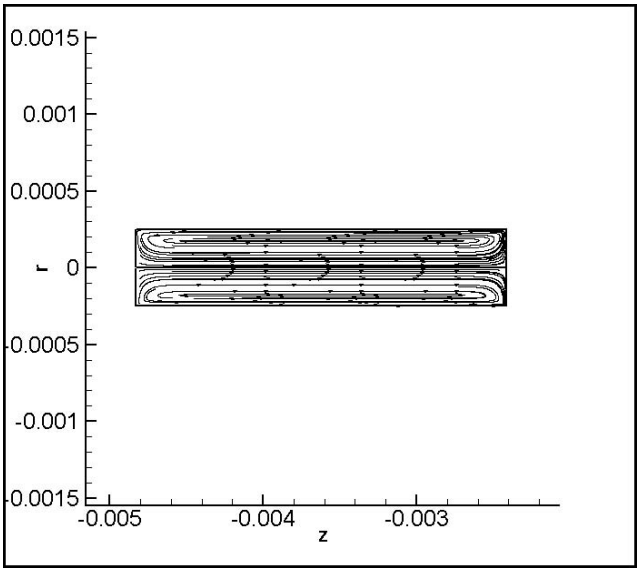

Figure 2.10. Streamline plot in one phase.

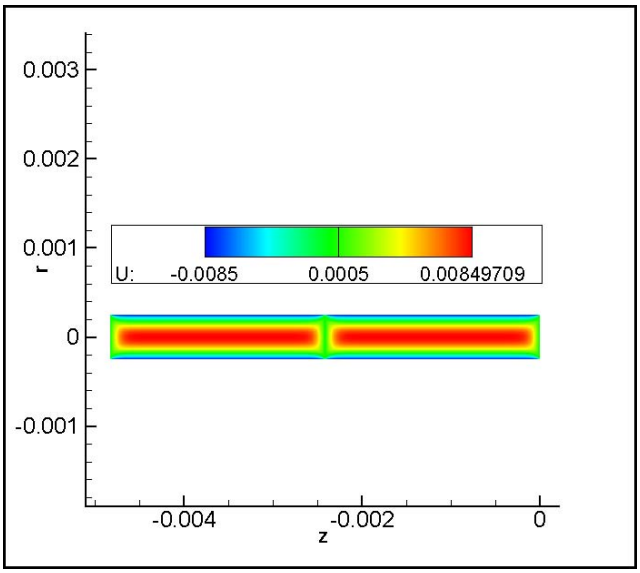

Figure 2.11. Velocity field.

With the assumption of fixed slug length and fixed channel size, the concentration profile was obtained for different average flow velocities in Fig. 2.12 and Fig. 2.13. It shows the time required to achieve 99% conversion of KOH. The plot clearly illustrate that the time required to reach 99% conversion of KOH decreases as the average flow velocity increases.

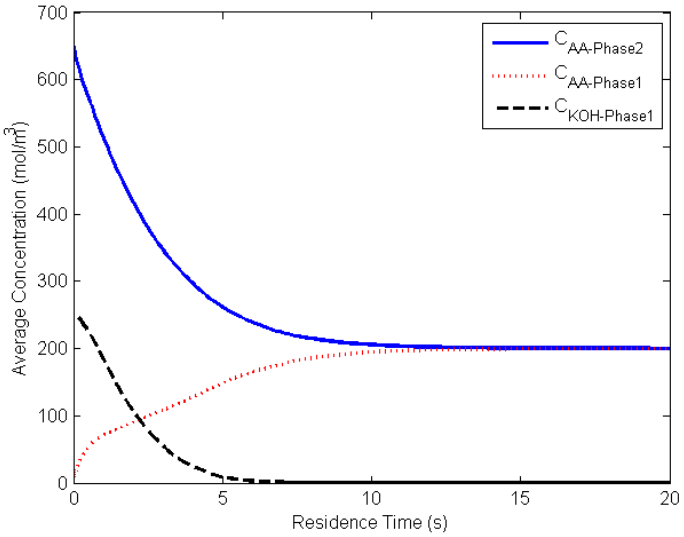

Figure 2.12. Concentration distribution of two reactants at an average flow velocity of 0.0042m/s.

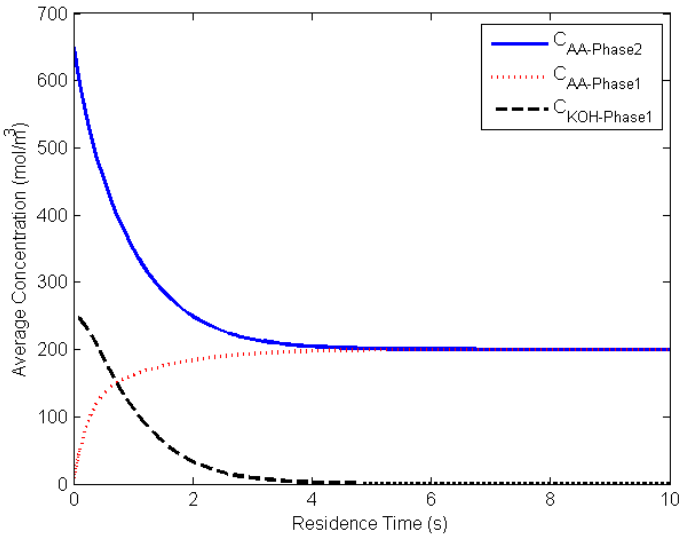

Figure 2.13. Concentration distribution of two reactants at an average flow velocity of 0.0142m/s.

To have better understanding of the mixing phenomenon within the reactions, the concentration distributions of AA in aqueous phase are plotted with different average flow velocities at same time stage, which are shown in Fig. 2.14 and Fig. 2.15. It clearly shows that the reaction only takes place in aqueous phase and it also indicates that AA achieves the equivalent concentration within both phases due to the excessive AA. It also shows that the AA is transported quicker with higher flow rate. On the other hand, the concentration of KOH in aqueous phase decreased rapidly during mass transfer within reaction under different average flow velocities, seen in Fig. 2.16 and Fig. 2.17. The KOH vanishes quicker with a higher flow rate, which is in good agreement with the experimental observation.

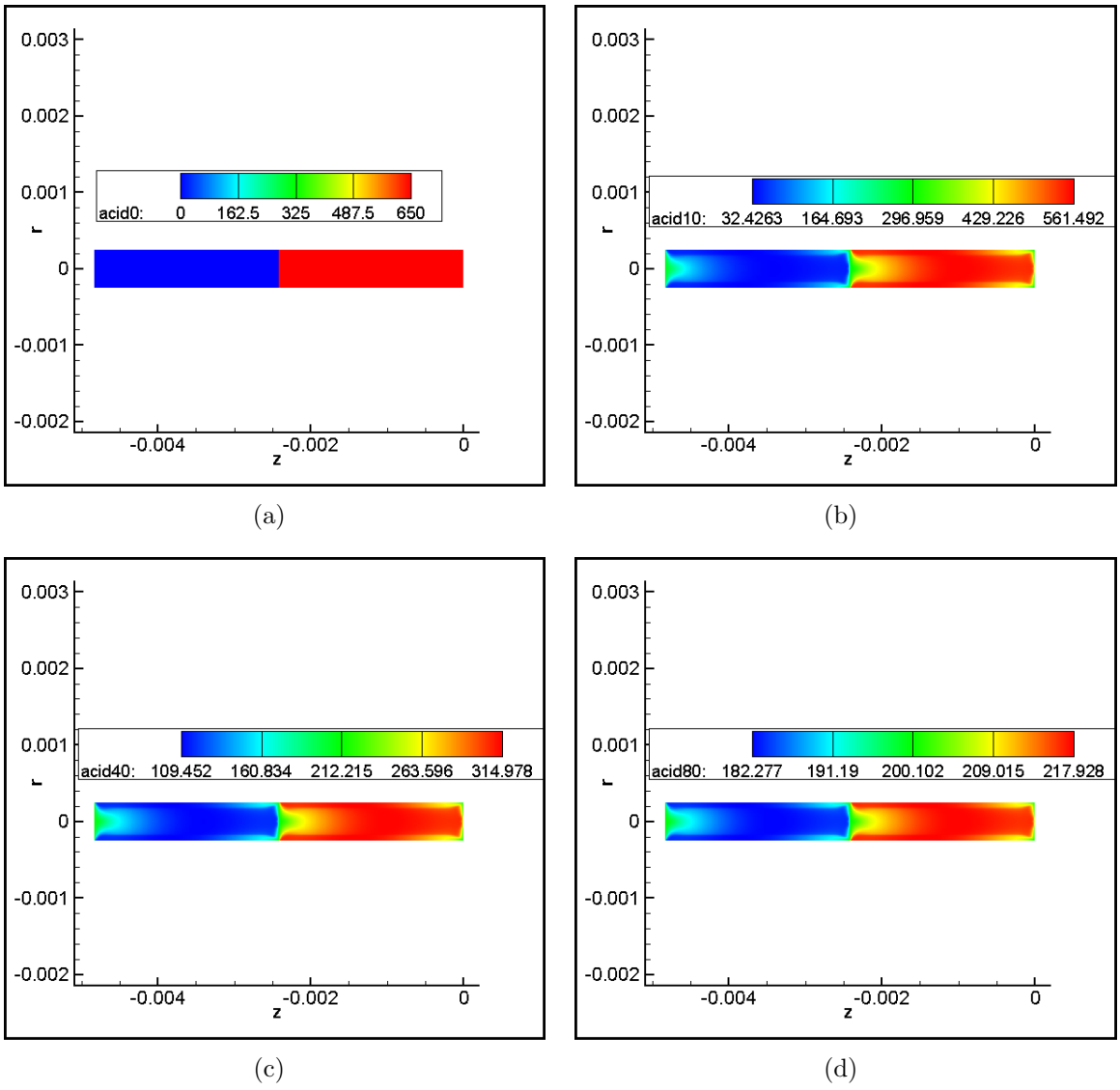

(a) (b)

(c) (d)

Figure 2.14. Concentration distribution of acetic acid in aqueous phase at an average flow velocity of 0.0042m/s at (a) t=0s, (b) t=1s, (c) t=4s, and (d) t=8s.

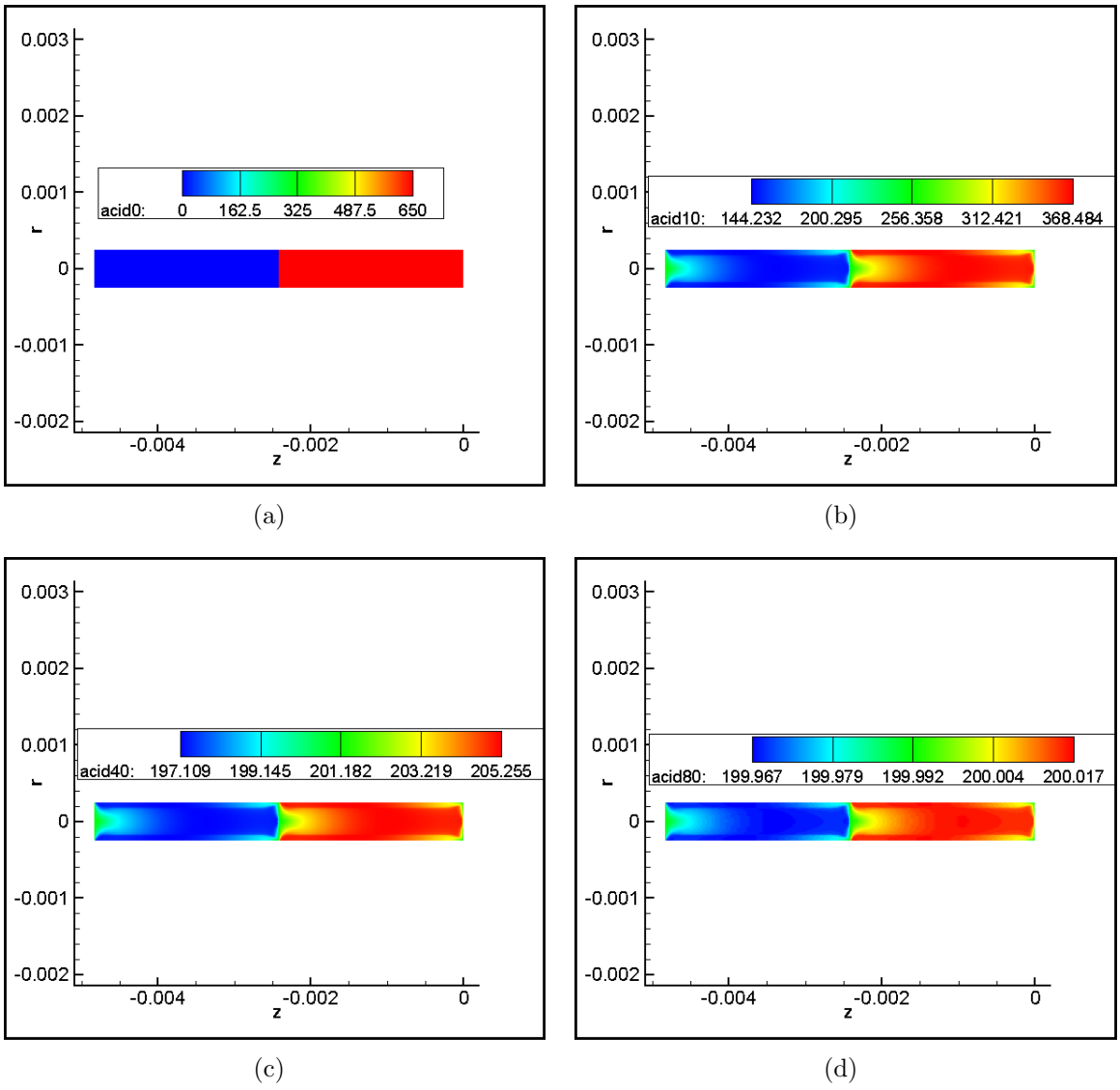

(a) (b)

(c) (d)

Figure 2.15. Concentration distribution of acetic acid in aqueous phase at an average flow velocity of 0.0142m/s at (a) t=0s, (b) t=1s, (c) t=4s, and (d) t=8s.

As seen in Fig. 2.14 and Fig. 2.15, with a low flow velocity of 0.0042m/s at t=1s, only about 4% of acetic acid transferred into aqueous phase; however, with a flow velocity of 0.0142 at t=1s, it is about 22% of acetic acid transferred into aqueous phase. At t=8s, acetic acid almost reaches a equilibrium state with higher flow velocity, but the concentration difference is still observed with a lower flow velocity.

Same prediction in KOH concentration variation for two different flow velocities, shown in Fig. 2.16 and Fig. 2.17.

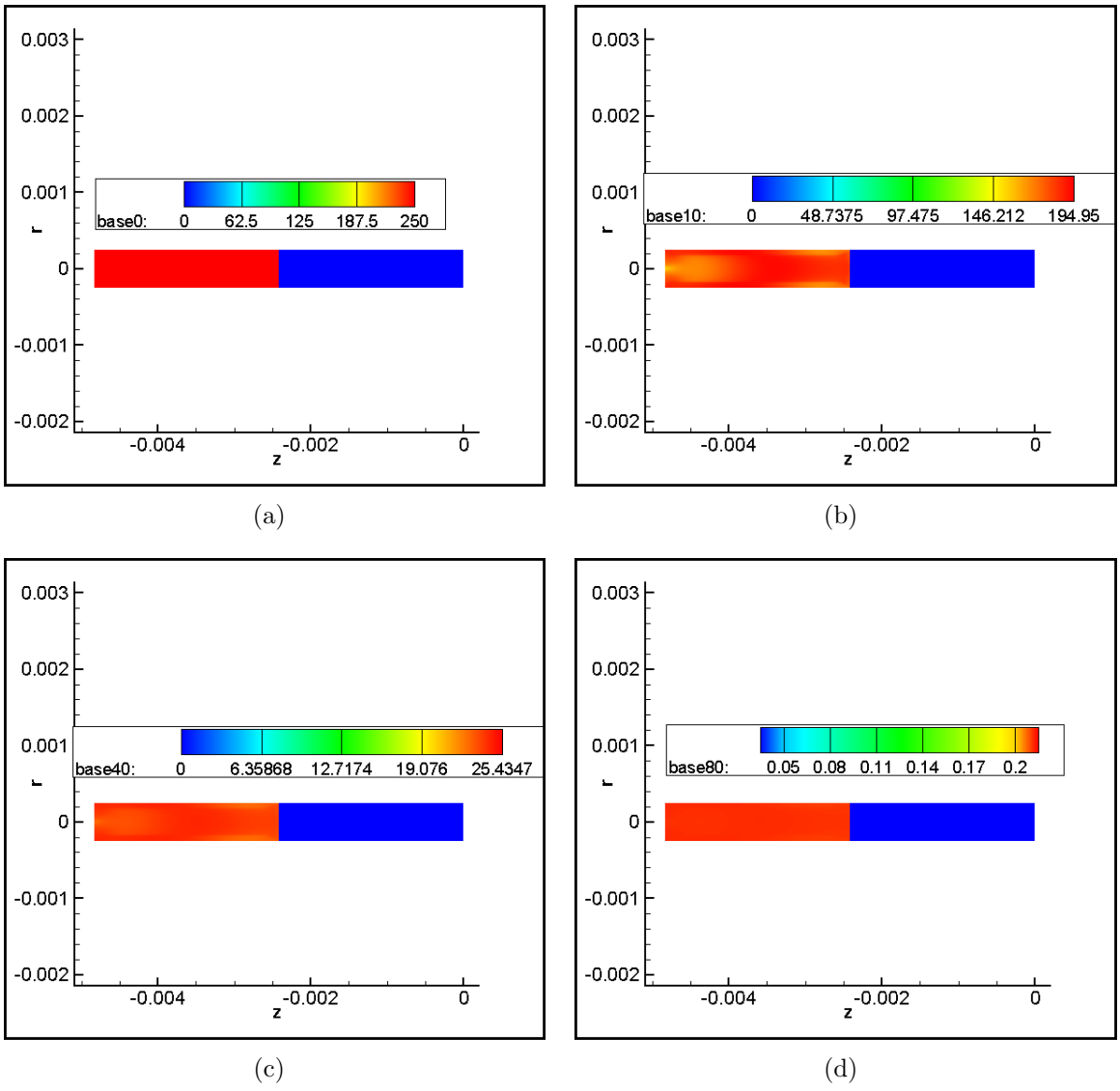

Figure 2.16. Concentration distribution of KOH at an average flow velocity of 0.0042m/s at (a) t=0s, (b) t=1s, (c) t=4s, and (d) t=8s.

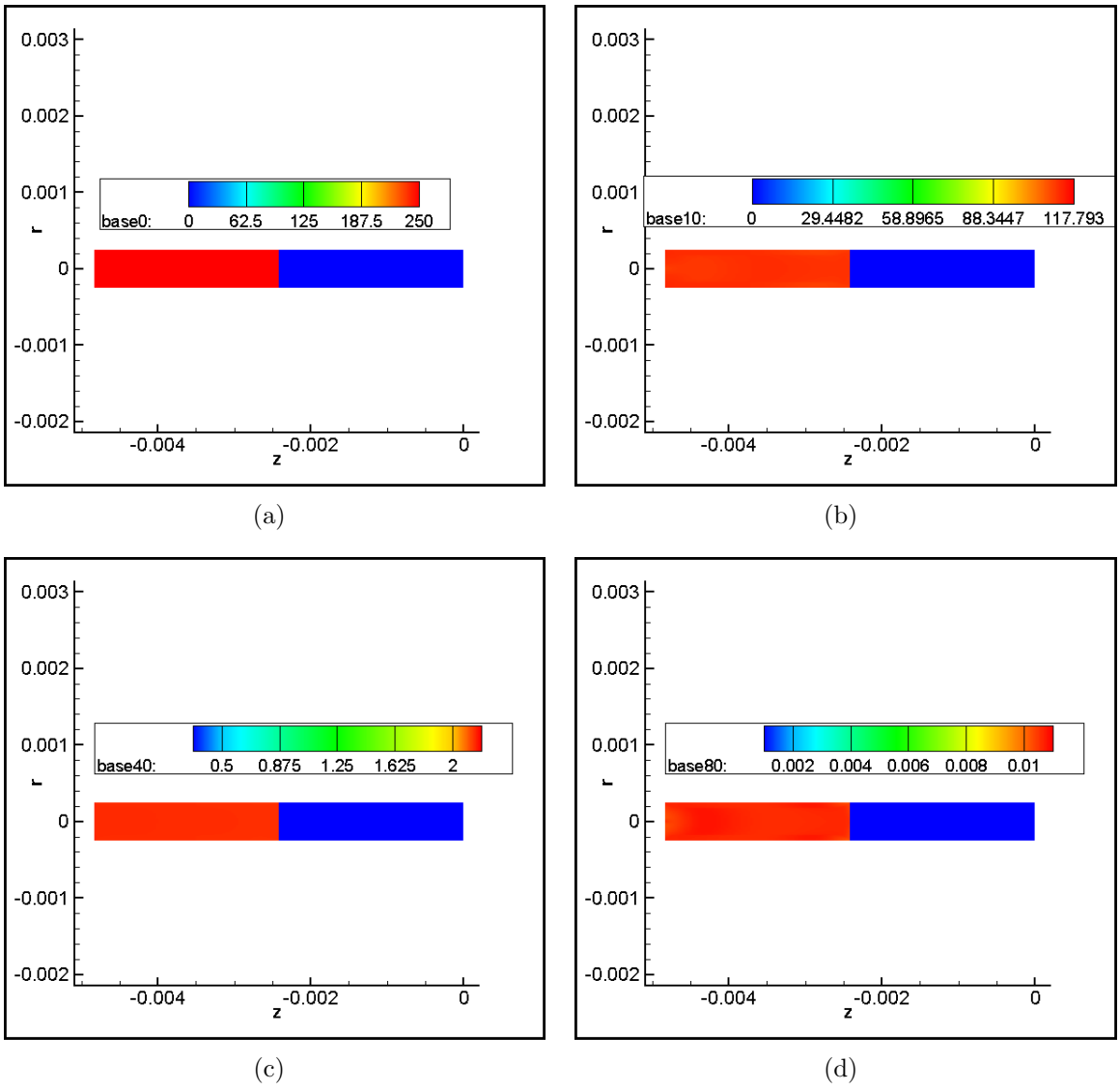

Figure 2.17. Concentration distribution of KOH with an average flow velocity of 0.0142m/s at (a) t=0s, (b) t=1s, (c) t=4s, and (d) t=8s.

As expected, about 22% of KOH is consumed at t=1s with a flow velocity of 0.0042m/s; however, at t=1s, almost 53% of KOH is consumed with a flow velocity of 0.0142m/s. At t=4s, only about 1% of KOH retains in aqueous phase. For a flow velocity of 0.0042m/s, about 10% of KOH remaining in aqueous phase. In

addition, concentration variation of acetic acid and potassium hydroxide over time with different average flow velocities is shown in Fig. 2.18, Fig. 2.19, and Fig. 2.20

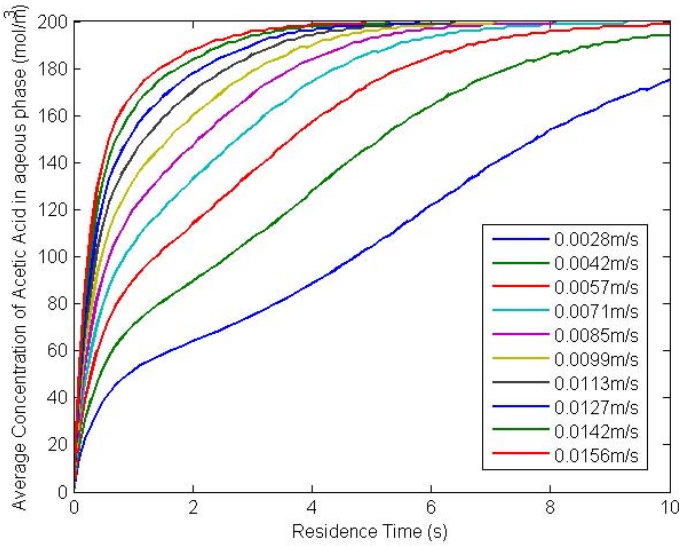

Figure 2.18. Concentration variation of acetic acid in aqueous phase with different average flow velocities.

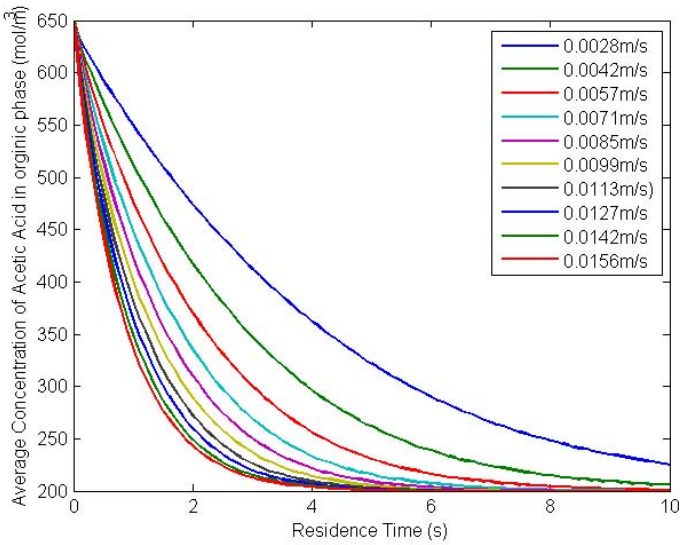

Figure 2.19. Concentration variation of acetic acid in organic phase with different average flow velocities.

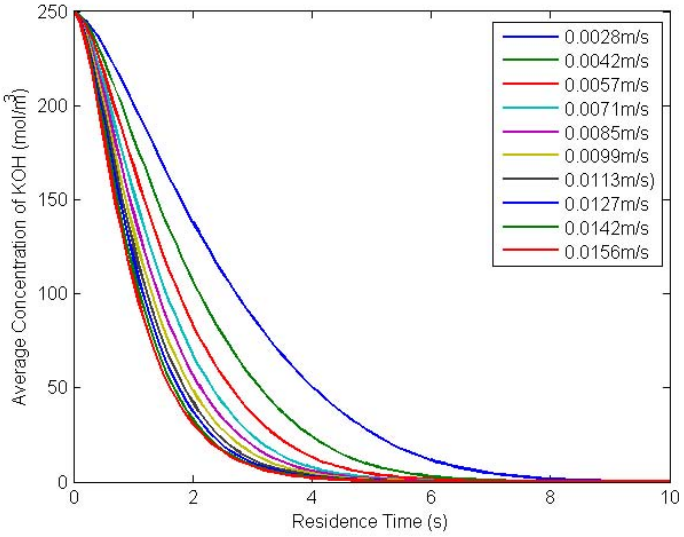

Figure 2.20. Concentration variation of KOH over time with different average flow velocities.

It shows a strong effect of flow rate on mixing efficiency. With higher flow velocities, the exponential change in concentration of each species is predicted, that also shows a significant contribution of convection to the mixing efficiency. Residence time is also reduced while having higher reactants conversion with higher flow velocities.

2.4 Evaluation Rate Constant k

For all the previous studies, the rate constant is evaluated by coupling simulation with optimization. Due to the complexities in finding the rate constant experimentaly, an optimization method is implemented to evaluate the rate constant. Because of the simplicity of the problem itself, interval halving 1-D searching scheme was used for this problem. The optimization approach was based on minimizing the error between simulation results and experimental data, seen in Fig. 2.21. For this problem, the rate constant k is the only design variable. The objective function is defined as Eqn. 2.7.

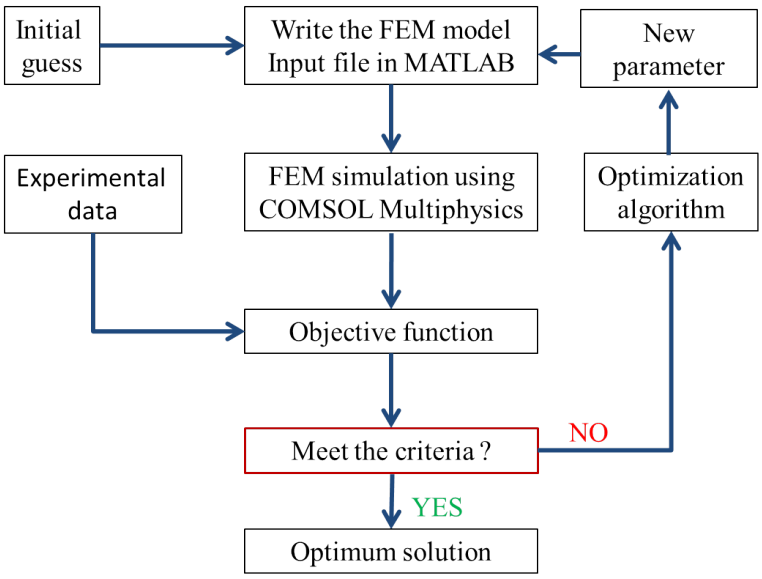

Figure 2.21. The schematic flowchart of the optimization algorithm.

$$Obj = \sum_{i=1}^{n} \left(\frac{t_{exp} - t(k_j)_{sim}}{t_{exp}} \right)^2 \tag{2.7}$$

Initial guesses were made to obtain the range of the k value by matching the simulation results with experimental data for different average flow velocities, providing the upper bound and lower bound of the design variable. The interval halving method was implemented into the optimization framework. The optimization stops until it meets the criteria. The optimum k was found as $0.0069 \mathrm{m}^3\mathrm{mol}^{-1}\mathrm{s}^{-1}$. The comparison between experimental data and simulation results is shown in Fig. 2.22.

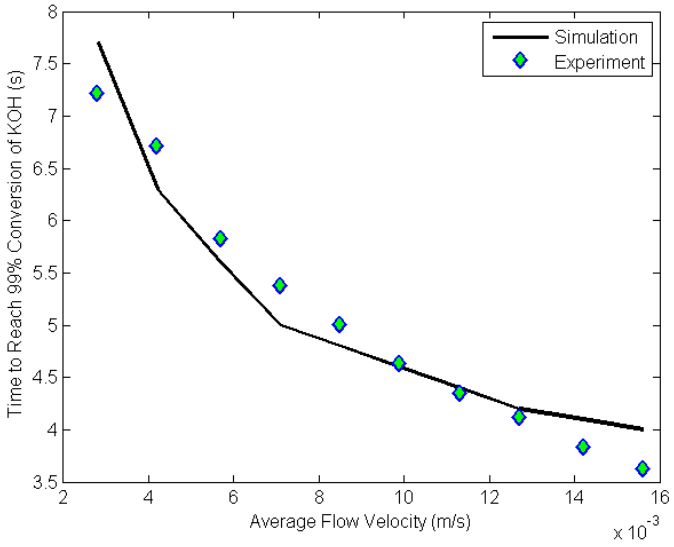

Figure 2.22. Comparison between experimental data and simulation results with the optimum rate constant.

2.5 Conclusions

As expected, the mixing time for passive mixing is decreased dramatically when compared with pure diffusion. With the formation of internal circulation within both slugs, the mass is not only transported by diffusion across the interface, but, convective mixing is also involved. With the internal circulation, the interfacial area

between two phases is increased and the interfacial concentration is renewed rapidly; furthermore, the molecular diffusion performance is also increased due to the smaller diffusion path within the internal circulation.

Based on the experimental results, it clearly shows that the AA is transported into the aqueous phase and the majority of the reaction takes place within the aqueous phase. Due to the excess amounts of AA, the concentration of AA will not vanish on both phases. The concentration of AA approximately becomes the same in the two phases when the reaction is close to the equilibrium state.

On the other hand, from the experimental observations, it indicates that reaction is getting slower towards to the end of reaction. The concentrations of the two reactants are both decreasing along with time, which cause the decrease of reaction rate. Therefore, it will take a longer time to reach the equilibrium state after the reactants conversion reached a certain level.

Additionally, different average flow velocities were applied for a fixed channel size. With the results comparison between high flow rate and low flow rate, it shows that rapid mixing will be obtained with higher flow rate. It is concluded that the mass transfer is mainly dominated and a higher reactants conversion can be done in a short time.

The mass transfer with chemical reaction in a microchannel has been studied using a simple experimental demonstration and a CFD simulation using with COMSOL Multiphysics package. The objective is to investigate the effect of different average flow velocities on the mass transfer with two-phase slug flow. Several simulation cases were carried out for performing the mass transfer behavior under different assumptions. The experimental results and numerical simulation results both indicate that the significant influence of flow velocity on mixing efficiency. At the same time,

the rate constant of reaction between AA and KOH is predicted by combining the experimental data and simulation results.

CHAPTER 3

INVESTIGATION OF MASS TRANSFER IN A GAS-LIQUID PHASE MICROREACTOR

3.1 Evaluation of Membrane A Microreactor for Gas Exchange

3.1.1 Introduction

Porous membranes have been widely used in different types of devices for gas exchange, separation, absorption, ultrafiltraition, and purification. Gas transport phenomena is of higher interest in a multiphase system. The most common gas exchange, which occurs in the biological system, is the CO_2 and O_2 exchange through capillary blood vessels in the respiratory system. This type of gas exchange is interesting because of the gas transfer through vessel wall which has lead to a numerous experimental and numerical studies concerning gas transport through porous materials.

Membranes are the most common material to use for gas selective and separation. Most conventional membranes are made of thin metal sheet. In a review conducted by Mansourizadeh and Ismail [30], they found that they could substitute the conventional solid membrane that exhibits low permeability and low efficiency with a polymeric microporous membrane. They mainly focused on the application of hollow fibre membrane. In general, the gas transport through a membrane always involves two phases: liquid phase and gas phase. Most of the liquid-gas contacting systems involve a chemical reaction process. The earliest application of gas-liquid contacting system was the blood oxygenator using hydrophobic microporous membrane which was made of polytetrafluoroethylene (PTFE) in 1975 [31]. Another polypropy-

lene (PP) microporous hollow fiber membrane was evaluated in vitro and in vivo for oxygenator application [32]. Later on, these types of liquid-gas membrane contacting system were gradually used in more applications; the two major applications were gas exchange in oxygenator and acid gas clean-up. In the past two decades, the hollow fibre membrane has drawn more attention for investigating the mass transport during gas transfer with an aqueous absorbent. This type of gas-liquid contactor offers several prevailing advantages over the conventional gas-liquid transport system:a large ratio of surface to volume; independent flow rate control for liquid phase and gas phase; easy to handle low flow rate; easy to scale up to hold higher flow rate; easy to maintain isothermal condition; flexible to change the interfacial area. A number of studies were conducted on mass transfer of O_2 and acid gas CO_2, SO_2, and H_2O by using the hollow fibre membrane contactors.

Qi and Cussler [33] developed the prototype of the hollow fibre contactor using a microporous non-wetted polypropylene (PP) membrane to absorb carbon dioxide by using an aqueous sodium hydroxide solution as the solvent. Lee et al. [34] experimentally built a hollow fibre membrane model and mathematically stated the non-linear partial differential equation to evaluate the reaction rate and equilibrium constants of the reaction between carbon dioxide and potassium hydroxide. Svitek and Federspiel [11] established a mathematical model to predict the CO_2 removal by using a bundle of hollow fibre membranes and formed the correlation of mass transfer for gas exchange between CO_2 and O_2. Dindore and Versteeg [35] carried out the absorption experiment with gas-liquid cross-flow using a hollow fibre membrane without a chemical reaction and mainly focused on the influence of the flow rate on the mass transfer model. Recently, Marjani and Shirazian [36] studied the gas transport of acid gas sulfur dioxide SO_2 through ceramic tubular membranes; they also used CFD simulation to predict the concentration distribution of SO_2 across the membrane.

Another type of gas-liquid membrane contacting system consists of a flat membrane. The experimental and theoretical study conducted by Zhang et al. [37] presented different diffusion phenomena through a flat miroporous membrane due to membrane pore structure. The flat membrane was also used by Zou et al. [38] to remove CO_2 from the fuel cell hydrogen processing. This type of membrane was also used for micro scale gas-liquid syntheses for the study of yield, selectivity and reaction time in a microchemistry system [39]. The dependency of the flow rate, catalyst loading, flow unit size, membrane material, membrane pore size, and fluids diffusivity were studied by Zou et al. [38], Dindore et al. [35], and Franco et al. [40]; they all emphasized the significant effect of these factors on the mass transport efficiency.

In most gas-liquid membrane contacting systems, the chemical reaction process is involved with the mass transfer. To increase the mass transfer efficiency, researchers have focused on the studies of different chemical solvent, the mass transfer rate of gas through the membrane, the flow rates of feed gas, and the characteristic of different types of membranes. Drioli et al. that polymeric material is preferable for gas permeation [41]. Most polymeric membranes are composed of interlaced microfibres and micropores. The surface property of these microporous membranes is either hydrophobic or hydrophilic, which is related to water morphology. Since the chemical reaction is involved in the gas transport process, the solvent should be highly active to the gas and chemically resistant to the membrane.

Qi and Cussler [42] found out that the big resistance for gas transport is the wetting membrane. In Nagy's book [43], which is the theoretical study of mass transfer through membranes, he summarized the wetting phenomena of hydrophobic and hydrophilic membranes with different phases. The phase distribution on different types of wetting membranes is illustrated in Fig. 3.1 [43].

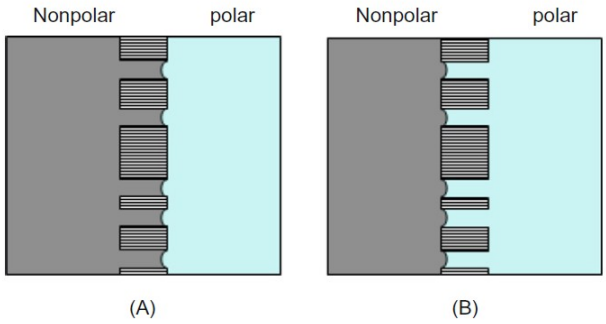

Figure 3.1. The wetting of hydrophobic (A) or hydrophilic (B) membranes by non-polar or polar phases respectively [43].

The liquid filling becomes one of the reasons to decrease the mass transport efficiency. Keshavarz et al. [44] developed the mathematical model to describe the absorption of acidic gas using a diethanolamine (DEA) aqueous solution in a hollow fibre membrane contactor; they also studied the partial wetting effect on the mass transfer through a microporous membrane and claimed that the partial wetting and liquid-filled pores have negative effect on mass transfer efficiency. Therefore, the choice of the membrane and solvent becomes very important to gas transport. The membrane should prevent wetting to ensure permeability. By using an aqueous solution for the solvent, the hydrophobic polymeric membranes are favourable material for gas transport through a membrane [45]. Polypropylene (PP), polyvinylidene fluoride (PVDF), and polytetrafluoroethylene(PTFE) are good choices for hydrophobic materials [46].

To characterize the wettability of a hydrophobic microporous membrane, the breakthrough pressure $\triangle p_{br}$ can be estimated using Laplace-Young equation [47]. The breakthrough pressure decides that if aqueous solutions can pass through the micropores freely and wet the fresh membrane. In other words, the aqueous solutions can not penetrate into a fresh membrane until the pressure difference between two

phases are larger than the breakthrough pressure. The breakthrough pressure is determined by micropore size, surface tension of solutions, and contact angle of the membrane, seen in 3.1 [47].

$$\triangle p_{br} = -\frac{4\gamma_l \theta}{d_m} \tag{3.1}$$

$\triangle p_{br}$ is the breakthrough pressure (Pa); γ_l is surface tension of the solutions (Nm^{-1});θ is the contact angle between the solutions and the memebrane $^\circ$; d_m is the diameter of micropores (m).

3.1.2 Motivation

The characterizations of gas absorption through hollow fibre membranes have been well studied throughout research. The gas transport mechanisms have been demonstrated experimentally and numerically for different types of membrane. To characterize the performance of a flat in-house made microporous PTFE membrane in a gas-liquid transport system, the mass transfer of CO_2 and O_2 with a chemical reaction were quantified with the microchannel design provided by Dr. Zeynep's lab. It should be noted that the microchannel pattern has been modified and simplified in order to cut down the effort of fabrication and assembly. The methods we proposed were simple and easy to carry out. In the following section, more details are provided.

The major goal of studying this type of membrane microreactor was to perform an experimental evaluation of the microporous membrane combined with microchannels for gas transport. The experimental results provided concrete proof-of-principle data that validate the design work done previously. Specifically, we aimed to determine the mass transfer coefficients for O_2, CO_2 and pressure-flow characteristics. At channel level, Sherwood number would be correlated with Reynolds/Schmidt number to characterize the overall system gas transport performance.

This portion of the project was divided into several subtasks. First, the microchannels and microporous membrane were fabricated specifically for the experimental testing. Next, the packaging for the microchannel/membrane was designed, fabricated, and assembled into the test microporous membrane microreactor. A test loop was then constructed and an experimental protocol defined. Finally, the data was collected and results were evaluated. More details regarding these subtasks will be given in the sections below.

Several design criteria need to be considered before constructing the gas-liquid membrane microreactor. At first, to enhance mixing efficiency in a multiphase system, smaller diffusion length is desired. Therefore, microchannel depth could be reduced. Additionally, second flow can be induced by modifying microchannel structure in order to increase mixing efficiency. Increasing residence time and driving force also can enhance mixing efficiency. Secondly, the selected membrane should have pore size in a micro scale or nano scale; it also needs to be able to hold a certain level of pressure. The durability of membrane needs to be considered for reducing material cost and ensure experimental consistency. Thinner membrane is preferred to reduce membrane resistance to mass transfer efficiency. Additionally, the membrane support design should ensure less damage of membrane with a chaotic flow and high pressure gradient across the membrane. At last, the flow rate on the liquid side needs to be adjusted to reduce boundary layer resistance to mixing efficiency.

3.1.3 Membrane Microreactor Design and Fabrication

The the preliminary and the main component of membrane microreactor is the membrane. The membrane we used was made of PTFE. As mentioned in the previous section, PTFE is a type of hydrophobic material which was suitably adaptable for this gas transport testing. After comparing different types of polymeric flat sheet

microporous membranes; Franco et al. [40] found that all types of polymeric membranes get at least partially wetted, but PTFE has large resistance to the in-depth wetting.

In this work, we also chose to use PTFE membrane, which consists of micropores. The scanning electron microscope (SEM) image of PTFE microporous membrane is shown in Fig. 3.2. The contact angle image of a deionized (DI) water droplet on the testing membrane is shown in Fig 3.3. The approximated micropores length was about 15μm-30μm. The value of contact angle was measured by using DI water. To ensure the minimum effect of vaporization, each contact angle image was taken less than five seconds after the DI water droplet was placed on the platform. The average contact angle of the five measurements was 145°, which indicated a very strong hydrophobic capability. A large contact angle is one of the factors leads to a higher breakthrough pressure according to Eqn. 3.1 [47]. From the detailed SEM images of microporous membrane, it was found that the microporous membrane consisted of multiple layers of interlaced microfibers. This complex structure helped to sustain a certain level of pressure and enforce the stiffness of the membrane. In one given area of microporous membrane, it obviously showed that the total area of micropores were much larger than the total area of microfibers.

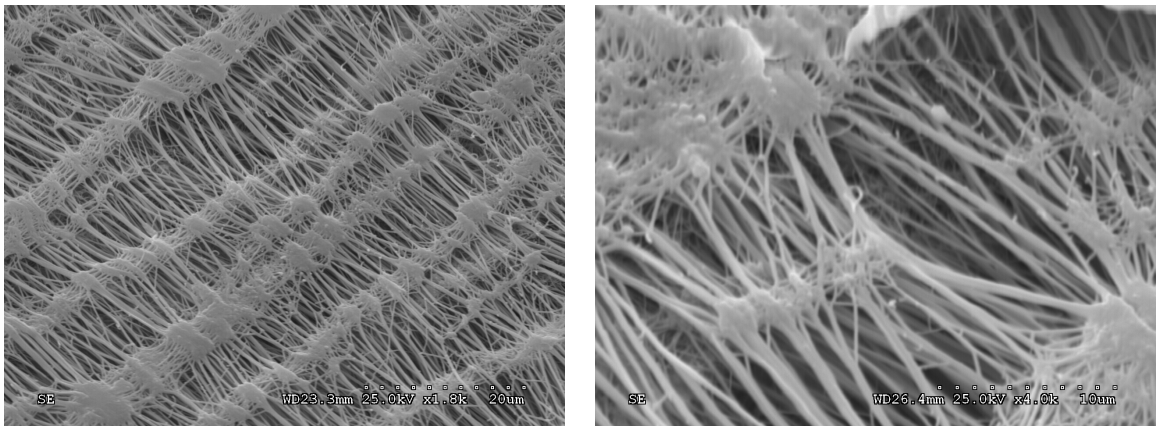

(a) (b)

Figure 3.2. (a) SEM image of PTFE microporous membrane; (b) A close-up view of PTFE microporous membrane under SEM.

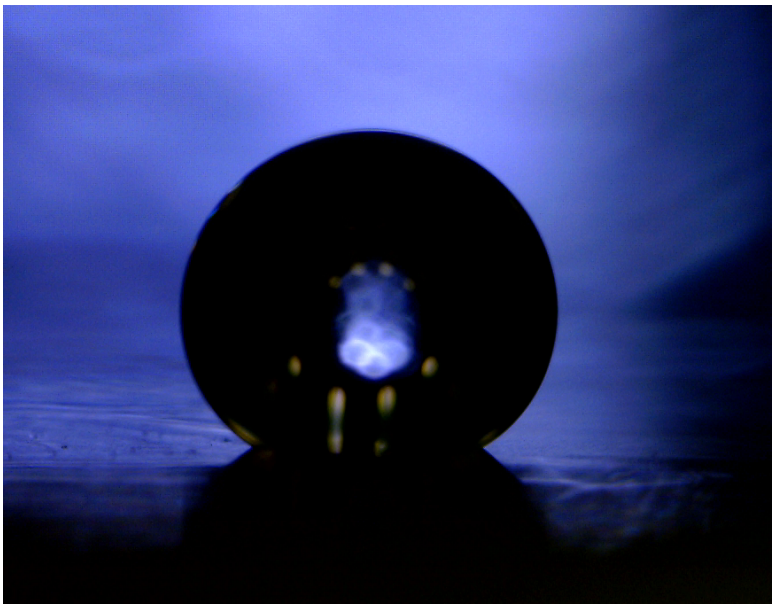

Figure 3.3. Contact angle measurement image of PTFE membrane.

The next major component was the microchannel. Based on the previous design work done by Bhargav Nabar from electrical engineering, NanoFab at UTA, we

slightly modified the microchannel and manifold design to simplify the test geometry and reduce the experiment limitations. This allowed for easier fabrication and numerical modelling. The changes were made with a commercial computer aided design (CAD) software using the detailed design as a base. The test membrane microreactor was designed to be simple to fabricate using a laser micromachining center. The microchannel layout is shown in Fig. 3.4. The bifurcation / channel design has been done by Bhargav Nabar from electrical engineering, NanoFab at UTA. The current design has three levels of manifold and sixteen mirochannels. The width of each channel is 150μm and the length is 4.62 mm. The depth of the microchannel was the thickness of the polyester films for liquid side and gas side.

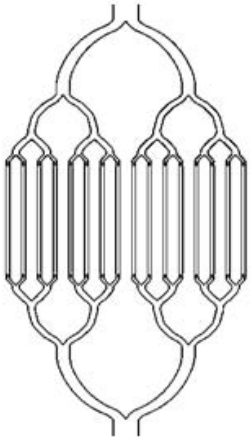

Figure 3.4. Modified design for testing; bifurcation / channel design has been done by Bhargav Nabar from electrical engineering, NanoFab, UTA.

The entire device was a laminated structure that consisted of a fixture and different layers of film cut-outs. An illustration of this is shown in Fig. 3.5.

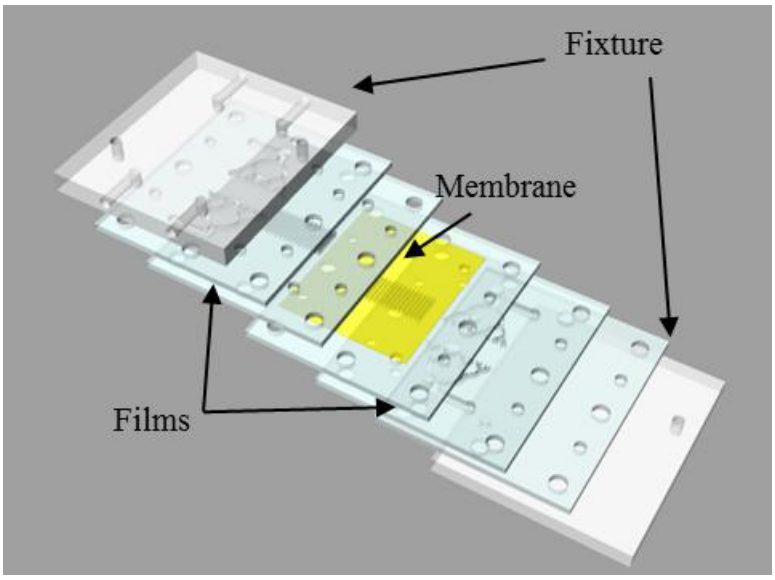

Figure 3.5. The 3D model of membrane microreactor.

A three-dimensional fluid path can be created by using multiple film layers. The fixture was a simple clamp that aligned and immobilized the layers. The depth of the features was controlled by the thickness of the film. Films compatible with our laser can be found as thin as 12.4μm, though 20μm thick films were the thinnest used in this work. It was possible to change the depth of features from one layer to the next by simply changing the film thickness. The manifold and channels were separated into two layers as shown in Fig. 3.6. The geometries were constructed and saved as a CAD file.

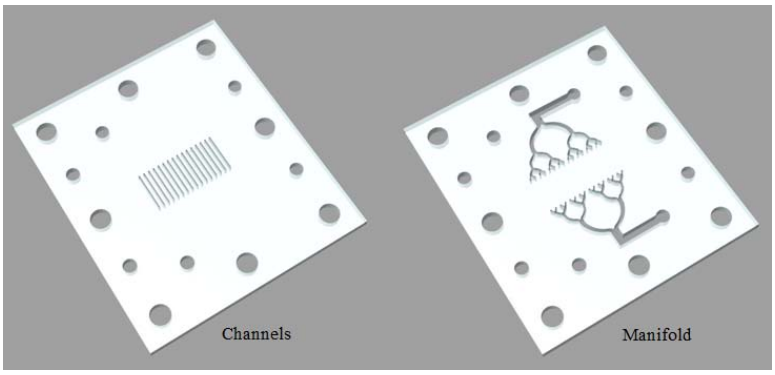

Figure 3.6. A rendered CAD model of the channel and manifold layer; bifurcation / channel design has been done by Bhargav Nabar from electrical engineering, NanoFab, UTA.

The CAD file was then converted to G-code using the Rhinoceros package, a commercial CAD system. The G-code was read directly by the laser micromachining center (Oxford Lasers Nd:YAG) and the pattern was cut into the film in approximately 30 minutes. In this work, we tried the following polymer films: polyester, polyimide (Kapton), and polycarbonate. Examples are shown in Fig. 3.7 and Fig. 3.8

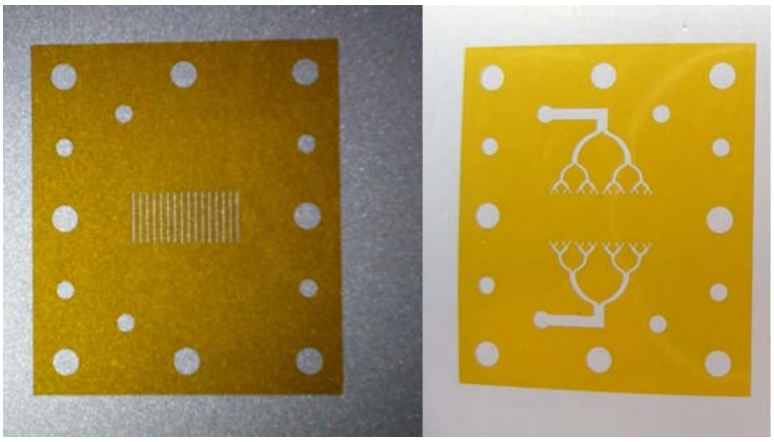

Figure 3.7. Manifold layer and microchannel layer laser cut in Kapton film with 20 μm thickness; bifurcation / channel design has been done by Bhargav Nabar from electrical engineering, NanoFab, UTA.

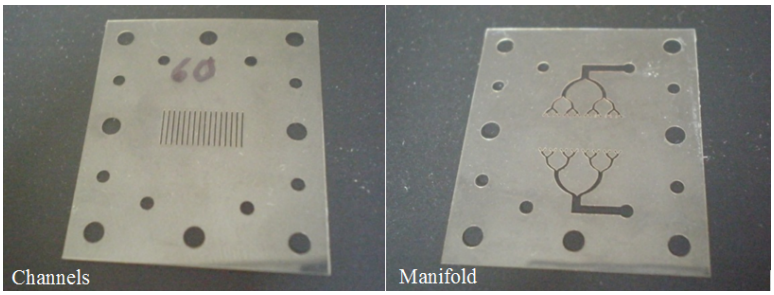

Figure 3.8. Manifold layer and microchannel layer laser cut in polyester film with 60 μm thickness; bifurcation / channel design has been done by Bhargav Nabar from electrical engineering, NanoFab, UTA.

The films were selected based on their transparency and machinability. During the experiment, a clear view of the channels was required, so materials that were opaque were not desirable. The material should also cut well with the laser; it should not crack, swell, or melt excessively near the edges of the cut. We found that Kapton gave the best cut and had sufficient clarity for very thin layers ($<50\mu$m). Thicker Kapton ($>60\mu$m) is a dark amber color and is difficult to see through so was not selected for use. Polycarbonate is clear and transparent so it was a candidate material for thicker layers. However, we found that while the polycarbonate could be cut with the laser, significant defects formed along the surface of the cut and made the parts difficult to seal.

3.1.4 Membrane Microreactor Testing Package

Once the manifold, exchange channels, and membrane were fabricated, an appropriate package was needed to hold the components together and to interface them with gas and liquid supplies of the test loop. In our case, we designed and fabricated a fixture and that includes fittings for capillary tubes. The fixture is made from polycarbonate and is held secure with 8 small bolts. The fixture can be assembled and

disassembled as desired. The CAD model and actual fixture are shown in Fig. 3.9. Note that the dimensions for the fixture and all film layers is 28.0 mm×32.0 mm.

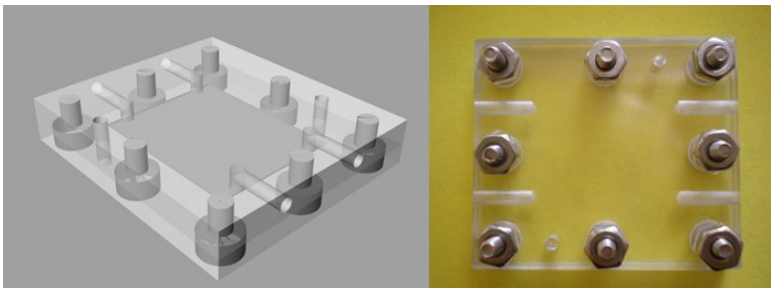

Figure 3.9. The CAD model and actual polycarbonate fixture package.

The manifold and channel layers for the liquid and gas sides were assembled, along with the membrane, into the fixture. An example of the complete test membrane microreactor assembly was shown in Fig. 3.10 and Fig. 3.11. Capillary tubes (not shown) are inserted into the holes in the side of the top portion of the fixture. These tubes deliver the liquids and gases at the rates required by the experiment protocol.

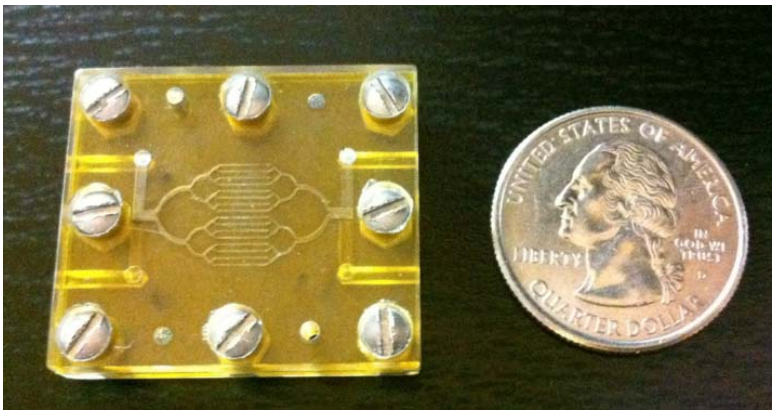

Figure 3.10. Membrane microreactor assembly.

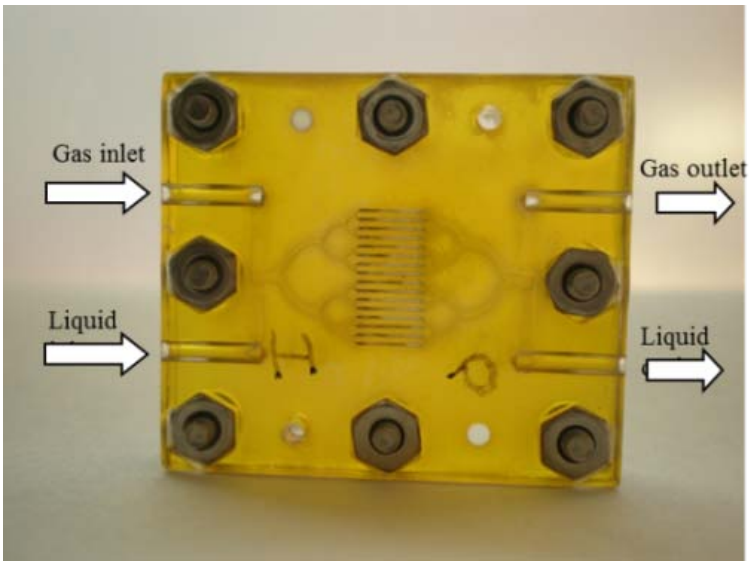

Figure 3.11. A schematic flow line.

3.1.5 Membrane Microreactor Test Loop

The mass transfer performance of membrane microreactor was of primary importance. Therefore, we designed a test loop and a test protocol for investigating gas transport through the membrane. For simplicity, we chose to work with distilled water as the liquid medium. We also chose to work with a single membrane, which equates to a single "layer". We essentially measure the amount of gas transferred across the membrane into the water running on the other side. This is illustrated in Fig. 3.12.

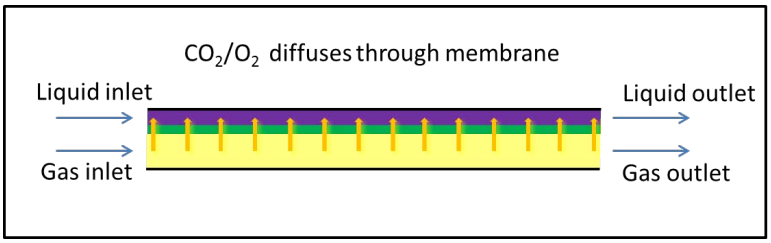

Figure 3.12. Illustration of O_2/CO_2 diffusion across the membrane in the experiment.

We noted that the volume of gas that was transferred to water for a single layer was too small to be measured indirectly by partial pressure measurements of the gas stream. Although this was a typical approach for high liquid volume flow rates (i.e. 5 L/min), we felt our pressure measurement instrumentation was not accurate enough for the low liquid flow rates (i.e. 2 mL/hr) in our experiment.

We therefore designed experiments based on simple chemical reactions in order to study gas transfer at low water flow rates. In addition, the experiments would be suitable for measuring gas transfer at different water Reynolds numbers. In the experiments, liquid and gas were both introduced through manifold inlets and flow along the microchannels where the mass transfer occurred. Liquid was flowing on the top channels and gas was running on the bottom as shown in the last figure. The flow of the liquid was observed through the top of the fixture during the experiment.

A test loop was designed and constructed to implement the experiment designs. The loop diagram is shown in Fig. 3.13. The flow rate of the water was precisely controlled by a positive displacement micropump. A flow meter was used to measure the flow rate of the gas to the microreactor, which was controlled by a precision meter valve. The CO_2 and O_2 were contained in standard size high pressure gas cylinders. Since the chemical reaction was involved into the mass transfer process, the same pH indicator detection technique used for slug flow study was capable to be applied to the gas-liquid reacting flow system.

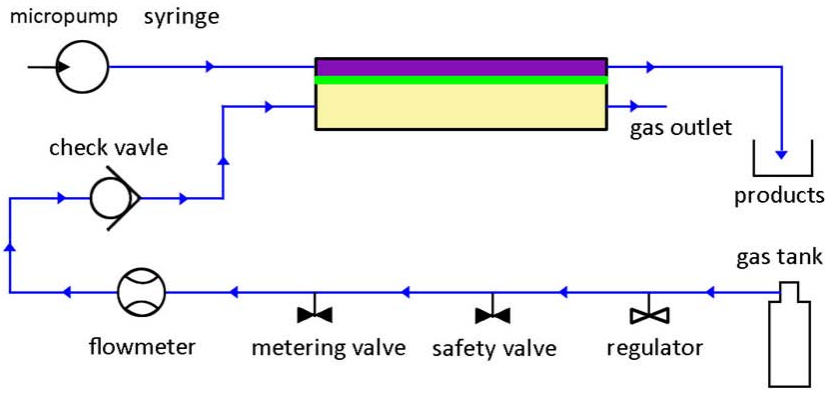

Figure 3.13. General test loop schematic diagram.

3.1.6 Mass Transfer Experiments for CO_2

A test membrane microreactor was fabricated for the CO_2 test. The details for the layers used as given in Table 3.1 and are counted from the bottom up. Note that the top layers are the water side and bottom layers are the gas side. The layers were assembled into the fixture and placed in the test loop. The assembly was then tested for leaks with dyed water and compressed air before starting the experiment.

Table 3.1. Detailed structure of membrane microreactor for CO_2 experiment

Layer #	Component	Material	Thickness, color
Layer 7	Fixture top	Polycarbonate	23.8 mm, clear
Layer 6	Manifold layer on liquid side	Polyester film	60 μm, clear
Layer 5	Microchannel	Kapton film	20 μm, yellow
Layer 4	Membrane	PTFE	No measurement, transparent
Layer 3	Microchannel	Kapton film	60 μm, clear
Layer 2	Manifold layer on gas side	Polyester film	125 μm, clear
Layer 1	Fixture bottom	Polycarbonate	31.8 mm, clear

Membrane microreactor performance testing was carried out with a reacting flow, which involves a reaction between potassium hydroxide aqueous solution and carbon dioxide in Eqn. 3.2

$$CO_2 + OH^- \xrightarrow{k} HCO_3^- \tag{3.2}$$

High purity carbon dioxide was used as the feed gas. The KOH aqueous solution was mixed with a pH indicator which was meta-cresol purple and loaded into the 5cc BD luer-lok^{TM} micropump. The solution was injected at specified flow rate and directed into the microreactor manifold by a transparent Teflon capillary tube. The initial filling process was monitored carefully to avoid the blockage of the water channels by air bubbles. The breakthrough pressure for PTFE microporous membrane can be estimated using the approximated micropores length, measured contact angle, and the surface tension of aqueous solution of potassium hydroxide. The surface tension of aqueous potassium hydroxide is $75.1\times10^{-3}\mathrm{Nm}^{-1}$ at 298 K according to Dunlap and Faris [48]. The estimated breakthrough pressure is in a range between 8.2 kpa to 16.4 kPa which is slightly larger than the pressure difference between two phases. It also explained that the membrane was partially wet after several experiments. However, there was no sever wetting or solution leaking through membrane during the experiment.

All experiments were carried out under room temperature and atmospheric pressure. The gas was flowing at a constant flow rate for all cases (7.66 ml/min). The indicator was initially purple and upon contact with the CO_2 beginning to change color in the downstream. If the flow rate was slow enough, the reaction will go towards completion and the outlet color will turn orange-yellow. This was illustrated in Fig. 3.14. Higher flow rates result in outlet water with a purple tint. One experimental

image showing pH color change zone is shown in Fig. 3.14. All flow rates achieved the color change were measured and recorded.

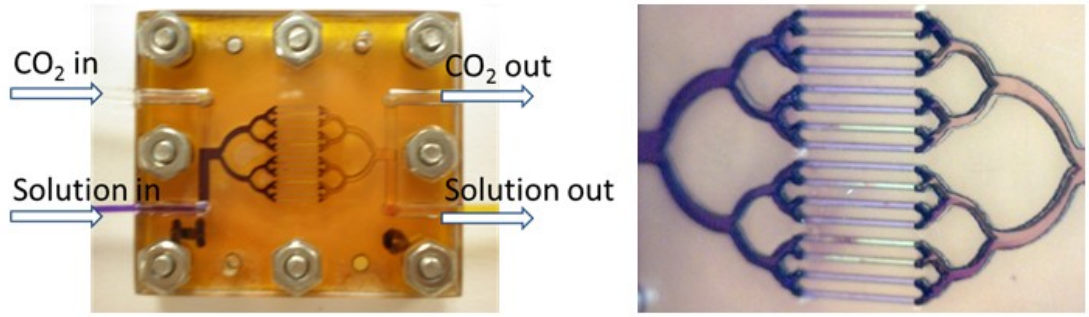

Figure 3.14. A picture of running experiment and the close-up view for CO_2 testing.

The Sherwood numbers which represents the ratio of convective to diffusive mass transport were then calculated based on the collected data. Reynolds number($Re = \frac{\rho v l}{\mu}$) was defined as the ratio of inertial to viscous forces and the Schmidt number ($Sc = \frac{\mu}{\rho D}$) represents the ratio of overall mass transfer to diffusive transport. The correlation equation in Eqn. 3.3 used is from S. R. Wickramasinghe et al. [49]. The results are tabulated in Table 3.2. We can clearly see the increase in Sherwood number while Reynolds number increases.

$$Sh = 0.8 Re^{0.59} Sc^{0.33} \tag{3.3}$$

$D_{CO_2-KOH} = 1.68\times10^{-}9m^2/s$ is the diffusion coefficient of CO_2 in potassium hydroxide, which can be calculated from Wilke-Chang correlation for binary system [28].

Table 3.2. Sherwood number dependence on Reynolds number

Channel Reynolds Number	Channel Sherwood Number	Total Sherwood Number
0.0084	0.4138	6.6202
0.0167	0.6228	9.9651
0.0334	0.9375	14.9999

3.1.7 Mass Transfer Experiments for O_2

As with the previous case, we assembled a membrane microreactor using film cut-outs and a membrane. The details were given in Table 3.3. All layers are counted from the bottom up. Note that we increased the depth of the channels on the oxygen side to reduce membrane deflection at higher gas flow rates. Additionally, the resistance of gas transport from gas side is much smaller than the liquid side, which allows to have large gas reservoir volume than the liquid side and also supplies excessive feed gas.

Table 3.3. Detailed structure of membrane microreactor for O_2 experiment

Layer #	Component	Material	Thickness, color
Layer 7	Fixture top	Polycarbonate	23.8 mm, clear
Layer 6	Manifold layer on liquid side	Polyester film	60 μm, clear
Layer 5	Microchannel	Kapton film	20 μm, yellow
Layer 4	Membrane	PTFE	No measurement, transparent
Layer 3	Microchannel	Kapton film	125 μm, clear
Layer 2	Manifold layer on gas side	Polyester film	125 μm, clear
Layer 1	Fixture bottom	Polycarbonate	31.8 mm, clear

We used a chemical reaction to determine the oxygen mass transfer across the membrane to flowing liquid. This turned out to be much more challenging than CO_2 case. We looked at three different reactions.

The first two reactions were based on the use of oxidation-reduction (redox) indicators. These indicators change colors as they were oxidized or reduced. The redox indictors, indigo carmine (IC) and methylene blue (MB), were selected as the reactants in aqueous solutions. In their oxidized forms, both compounds have a dark blue color. However, when they are reduced, they become colorless. In the presence of oxygen, an oxidation reaction will occur and the compounds will return to a blue color. As a result, the transfer of oxygen can be observed on the basis of color change.

However, those two cases were both given up due to several serious issues. The solubility of IC in water was not high enough. The solution began turning blue in the pump and the feed lines from exposure to oxygen in the air. The solubility of MB is slightly higher than IC, but we still had limited time to work with the reduced form before it oxidized with the surrounding air. This made it difficult to see a significant color change between input and output and thus difficult to make an accurate calculation of the mass transfer. In addition, the oxidized forms of IC and MB are aggressive stains and eventually started to diffuse into the membrane and the Kapton films. This staining would influence observation of the experiment. We concluded that the redox indicators were good for qualitative indication of oxygen transfer but could not be used for measurements without instrumentation for colorimetry.

Our third reaction was a catalyzed oxidation reaction. It was a simple oxidation reaction that has been widely used for deoxygenation in various industries. The reaction is expressed as follows in Eqn. 3.4.

$$2Na_2SO_3 + O_2 \overset{CaSO_4}{\rightleftharpoons} 2Na_2SO_4 \tag{3.4}$$

It was found that sodium sulfite (Na2SO3) was easily oxidized to sodium sulfate (Na2SO4) with a cobalt salt catalyst at room temperature and atmospheric pressure.

In addition, we found that the sulfite solution is basic and becomes neutral after it is converted to sulfate. This drop in pH value can be monitored with a color indicator using the same procedure as the CO_2 experiments. The sodium sulfite aqueous solution appearsed dark purple after adding a pH indicator then turned yellow when it was oxidized to sodium sulfate, thus signalling the end of the reaction.

As in the previous experiment, different concentrations of sodium sulfite solutions were prepared. The Na_2SO_3 solution mixed with the pH indicator and the cobalt sulfate ($COSO_4$) represented the liquid reactant. It was injected into the manifold inlet using the micropump. High purity oxygen was used as the feed gas and it was flowing under a constant flow rate (7.09 mL/min). Meanwhile, the flow rate of Na_2SO_3 was recorded when it was completely oxidized, which means the manifold outlet on the liquid side turns yellow Fig. 3.15. For higher concentrations of sulfite, a small amount of cobalt salt precipitates out and accumulates on the membrane causing some coloration Fig. 3.15. This can be eliminated in the future by using an appropriate buffer solution.

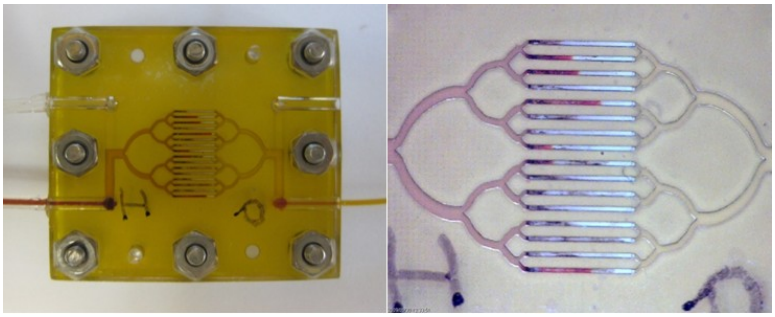

Figure 3.15. A picture of running experiment and the close-up view for O_2 testing.

As in the CO_2 case, a higher concentration of O_2 was realized at slower flow rates. Additionally, the Sherwood number was calculated for various Reynolds num-

bers and tabulated in Table 3.4. In this case, we found Sherwood number increased as Reynolds number increased, which followed a similar trend with the experimental results obtained by Goerke et al. shown in Fig. 3.16 [50]. Both results show an approximate linear relation between Reynolds number and Sherwood number.

Table 3.4. Sherwood number dependence on Reynolds number using 0.1M Na_2SO_3

Channel Reynolds Number	Channel Sherwood Number	Total Sherwood Number
0.0876	1.0528	16.8441
0.1314	1.3373	21.3965
0.1752	1.5847	25.3546
0.2189	1.8076	28.9224
0.2627	2.0129	32.2070
0.3065	2.2046	35.2736

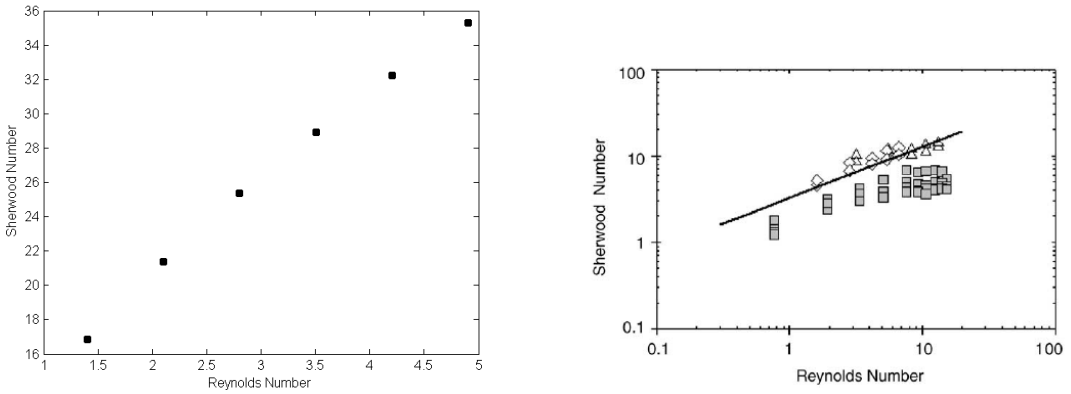

(a) (b)

Figure 3.16. A comparison of Sherwood number variation with literature data; (a) variation of Sherwood number with Reynolds number for oxygen transfer through PTFE microporous membrane, (b) variation of Sherwood number with Reynolds number for oxygen transfer in a membrane contactor [50].

As seen in Fig. 3.16, the literature image shows a comparison of experimental data of O_2 transfer through PTFE microporous membrane to an aqueous solution with a derived correlation from Goerke et al. [50]. An approximate linear relation is observed from their study. In the comparison, triangles and diamonds represent data for a characteristic length of 200 μm; while squares represent data for a characteristic length of 280 μm. The smaller characteristic length results in a better mass transfer performance. The characteristic length of our microchannel design is 20 μm. The calculated Sherwood number follows the same trend as the literature data, and it also shows that there is better mass transfer performance than literature data with lower Reynolds numbers and smaller characteristic length.

We believe the reduced mass transfer at the lower Reynolds number is an artifact of the experiment. The low Reynolds number data points correspond to higher concentrations of sulfite. At these higher concentrations we observed a portion of the catalyst precipitating out of the solution. This loss of catalyst would result in lower reaction rates for production of sulfate and a lower Sherwood number and cause partial wetting of the membrane. Based on this reason, the Sherwood value of 35.2736 should be the most accurate since it corresponds to the lowest sulfite concentration. If so, it indicates that the membrane microreactor is achieving higher mass transfer rates for O_2 compared to CO_2.

3.2 CO_2 Absorption Using a Membrane Microreactor

3.2.1 Introduction

Based on the previous gas transfer study, the detailed gas transfer through a flat PTFE microporous membrane was of interest. A new gas-liquid membrane mciroreactor was specifically designed for gas absorption application. The feed gas

we chose to use was high purity carbon dioxide. Carbon dioxide is one of the by-products of hydrogen production, production of renewable energy, production of fuel cell, and synthesis of gas. Carbon dioxide is also one of the well-known greenhouse gases. A number of studies have been carried out in few research institutes and research and development departments in industry for carbon dioxide capture and separation. Several commercial CO_2 capture systems have been developed in the market. However, a lot of researchers are still seeking new ways to increase the CO_2 capture efficiency, to reduce the cost, and to make it suitable for the on-site fuel generation [51],[52].

For the past two decades, some researchers have started using chemical reactions to demonstrate CO_2 transfer rate. The most common solvent they have used is carbonate salt aqueous solution, such as K_2CO_3 and Na_2CO_3 [53],[34],[54],[55]. At the same time, the reaction mechanism also has been well studied within different reactions. From a review of existing carbon dioxide technologies and solvent selection, it was concluded that the general and reliable way to capture CO_2 is through chemical absorption, which was widely studied by researches and used in industrial practice. In order to adapt to different working environment and scale requirements, different CO_2 capture techniques are still under development. In this work, we chose an alkaline aqueous solution as the solvent and used a flat PTFE microporous membrane to develop a type of microreactor for gas absorption. The membrane we chose to use was same as previous study. To monitor the reaction progression, we continuously used the pH indicator detection technique.

3.2.2 Reaction Mechanism of Carbon Dioxide in a Alkaline Aqueous Solution

CO_2 is a type of acidic gas and is easy to dissolve into water to form carbonic acid (H_2CO_3), a weak acid. However, the solvent we chose to use is the potassium hydroxide aqueous solution, a strong base solution. Therefore, it is not necessary to use a buffer solution to control the pH value change during the gas absorption. On the other hand, the pH value change will be used as the probe to monitor the reaction progression. When carbon dioxide dissolves into potassium hydroxide aqueous solution, there were various reactions talking place [56].

$$CO_2 + OH^- \underset{k_{1,2}}{\overset{k_{1,1}}{\rightleftharpoons}} HCO_3^- \tag{3.5}$$

$$HCO_3^- + OH^- \underset{k_{2,2}}{\overset{k_{2,1}}{\rightleftharpoons}} CO_3^{2-} + H_2O \tag{3.6}$$

Due to a large amount of hydroxide anion (OH^-), the reaction between CO_2 and OH^- was the preliminary step of CO_2 conversion. sequentially, a fast reaction between bicarbonate ion (HCO_3^-) and OH^- is taking place. As a result of the excessive amount of carbon dioxide, the following reaction occurs, seen in Eqn. 3.7.

$$CO_2 + CO_3^{2-} + H_2O \underset{k_{3,2}}{\overset{k_{3,1}}{\rightleftharpoons}} 2HCO_3^- \tag{3.7}$$

Along with these reactions, the carbonic acid formation occurred which is shown in Eqn. 3.8−3.10.

$$CO_2 + H_2O \underset{k_{4,2}}{\overset{k_{4,1}}{\rightleftharpoons}} HCO_3^- + H_3O^+ \tag{3.8}$$

$$HCO_3^- + H_2O \underset{k_{5,2}}{\overset{k_{5,1}}{\rightleftharpoons}} CO_3^{2-} + H_3O^+ \tag{3.9}$$

$$H_2O \underset{k_{w,2}}{\overset{k_{w,1}}{\rightleftharpoons}} H_3O^+ + OH^- \tag{3.10}$$

The first three reactions were the controlling reaction when carbon dioxide dissolves into alkaline aqueous solution. The first reaction is a second order reaction and practically irreversible. The second reaction only involves proton transfer and can be treated as an instantaneous reversible reaction [54]. Therefore, a number of carbonate ions (CO_3^{2-}) were produced immediately when the carbon dioxide dissolved into the alkaline aqueous solution, which resulted in a production of HCO_3^- with excessive CO_2. The overall reaction of carbon dioxide dissolving into alkaline aqueous solution leads to the following reaction, seen in Eqn. 3.11.

$$CO_2 + OH^- \longrightarrow HCO_3^- \tag{3.11}$$

The solubility product $K_w(mol^2/m^6)$ in Eqn. 3.12, was calculated by using correlation from Tsonopolous [57], is shown in Eqn. 3.13. The equilibrium constant of reaction shown in Eqn. (3.8), $K_4(mol/m^3)$ Eqn. 3.14, was taken from Sharma and Danckwerts [58] shown in Eqn. 3.15.

$$K_w = [H_3O^+][OH^-] \tag{3.12}$$

$$K_w = 10^{(-(\frac{5839.5}{T}+22.4743logT-61.2062))}\rho_w^2 \tag{3.13}$$

$$K_4 = \frac{[H_3O^+][HCO_3^-]}{[CO_2]} \tag{3.14}$$

$$K_4 = exp(\frac{-12092.1}{T} - 36.786ln(T) + 235.482)\rho_w \tag{3.15}$$

The equilibrium constant for reaction Eqn. (3.5), K_1 (mm^3/mol), can be represented by Eqn. 3.16. The equilibrium constant for reaction Eqn. (3.6) at infinite dilution, K_2 (m^3/mol) was taken from Hikita (Eqn. 3.19) [54] and Roberts and Danckwerts (Eqn. 3.18) [59]. Equilibrium constants for reaction Eqn. (3.7) and reaction Eqn. (3.9) are listed below.

$$K_1 = \frac{[HCO_3^-]}{[CO_2][OH^-]} = \frac{K_4}{K_w} \tag{3.16}$$

$$K_2 = \frac{[CO_3^{2-}]}{[HCO_3^-][OH^-]} \tag{3.17}$$

$$log\frac{K_2}{K_2^\infty} = \frac{1.01\sqrt{[K^+]}}{1+1.49\sqrt{[K^+]}} + 0.061[K^+] \tag{3.18}$$

$$logK_2^\infty = \frac{1568.94}{T} + 0.4134 - 0.006737T \tag{3.19}$$

$$K_5 = \frac{[HCO_3^-]^2}{[CO_2][CO_3^{2-}]} \tag{3.20}$$

$$K_5 = \frac{[H_3O^+][CO_3^{2-}]}{[HCO_3^-]} \tag{3.21}$$

According to Dindore et al. [35], reaction shown in Eqn. 3.5 is practically irreversible when the pH value is above 10, which is applicable to our study. The forward rate constant $k_{1,1} = 12.1 \times 10^3 M^{-1}s^{-1}$ was taken from [60]. Reaction Eqn. (3.6) is faster than reaction Eqn. (3.5). The forward rate constant for reaction Eqn. (3.6), $k_{2,1} = 6 \times 10^9 M^{-1}s^{-1}$, was taken from [55] by Cents et al. For the third rate controlling reaction Eqn.3.7, according to Astarita [61], the rate is primarily dominated by first reaction Eqn. 3.5 and the backward rate of second reaction Eqn. 3.6, which agrees with Hikita's conclusion [54]; $k_{3,1} = 1.22 \times 10^6 s^{-1}$ is taken from [55].

The complete system of reaction rates for each species are defined as follows

$$\begin{aligned} R_{CO_2} = &-k_{1,1}[CO_2][OH^-] + k_{1,2}[HCO_3^-] - k_{3,1}[[CO_2][CO_3^{2-}] \\ &+k_{3,2}[HCO_3^-]^2 - k_{4,1}[CO_2] + k_{4,2}[HCO_3^-][H_3O^+] \end{aligned} \tag{3.22}$$

$$\begin{aligned} R_{OH^-} = &-k_{1,1}[CO_2][OH^-] + k_{1,2}[HCO_3^-] - k_{2,1}[HCO_3^-][OH^-] \\ &+k_{2,2}[CO_3^{2-}] + k_{w,1} - k_{w,2}[H_3O^+][OH^-] \end{aligned} \tag{3.23}$$

$$\begin{aligned} R_{HCO_3^-} = &k_{1,1}[CO_2][OH^-] - k_{1,2}[HCO_3^-] - k_{2,1}[HCO_3^-][OH^-] \\ &+k_{2,2}[CO_3^{2-}] - k_{3,2}[HCO_3^-]^2 + k_{3,1}[[CO_2][CO_3^{2-}] + k_{4,1}[CO_2] \\ &-k_{4,2}[HCO_3^-][H_3O^+] - k_{5,1}[HCO_3^-] + k_{5,2}[CO_3^{2-}][H_3O^+] \end{aligned} \tag{3.24}$$

$$\begin{aligned} R_{CO_3^{2-}} = &k_{2,1}[HCO_3^-][OH^-] - k_{2,2}[CO_3^{2-}] - k_{3,1}[[CO_2][CO_3^{2-}] \\ &+k_{3,2}[HCO_3^-]^2 + k_{5,1}[HCO_3^-] - k_{5,2}[CO_3^{2-}][H_3O^+] \end{aligned} \tag{3.25}$$

$$\begin{aligned} R_{H_3O^+} = &k_{w,1} - k_{w,2}[H_3O^+][OH^-] + k_{4,1}[CO_2] - k_{4,2}[HCO_3^-][H_3O^+] \\ &+k_{5,1}[HCO_3^-] - k_{5,2}[CO_3^{2-}][H_3O^+] \end{aligned} \tag{3.26}$$

When CO_2 dissolve into an aqueous alkaline solution, it is highly reactive with OH^- other than with H_2O at a high pH value. This was also investigated by Wang et al. [60], they concluded that the reaction rate between CO_2 and OH^- is about 10^7 times higher than the reaction rate between CO_2 and H_2O. Therefore, reactions of Eqn. 3.8 and Eqn. 3.9 were assumed to be negligible during this absorption process. The reaction rate system for each species can be simplified by eliminating the contribution term from Eqn. 3.8 and Eqn. 3.9.

3.2.3 Membrane Microreactor Design and Fabrication

To experimentally investigate the gas transport and to evaluate the microporous membrane reaction performance along with gas transport, we designed, manufactured, and assembled a membrane reactor prototype. The prototype we used was a micro scale membrane reactor. It consisted of a flat PTFE microporous membrane, fixture, and two microchannels which both had a width of 500μm and a depth of 250μm. The purpose of having a fixture was to immobilize the microchannel and to enforce an enclosed flowing environment. Microchannels were made out of polycarbonate, same as the fixture. All the parts were made by the means of micromachining in the machine shop at The University of Texas at Arlington. Two microchannels were lined in parallel to each other and a flat PTFE microporous membrane was placed in between two channels. Two pieces of microchannel plates were bonded together with the fixture using screws.

A Micorporous PTFE membrane was selected due to the hydrophobic characteristics which were described in the previous section. The PTFE membrane has matrix-like porous structure. SEM images of a single layer microporous membrane are shown in Fig. 3.17 and Fig. 3.18.

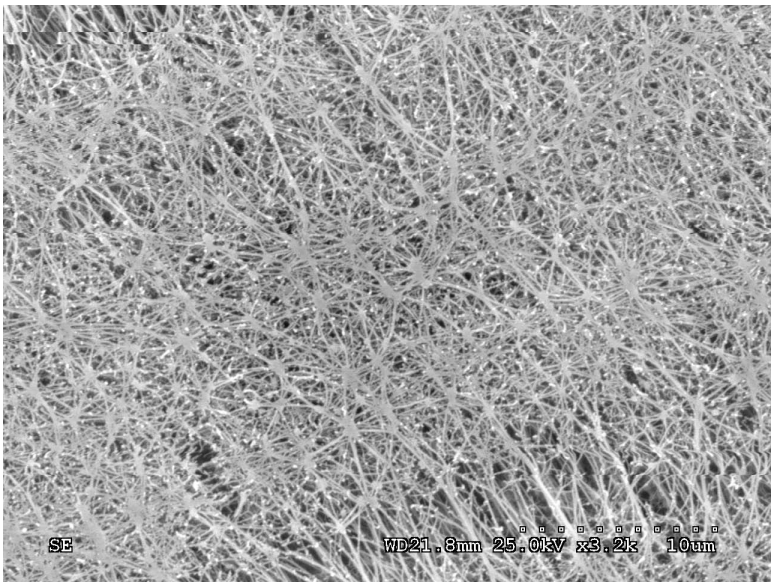

Figure 3.17. SEM image of PTFE microporous membrane.

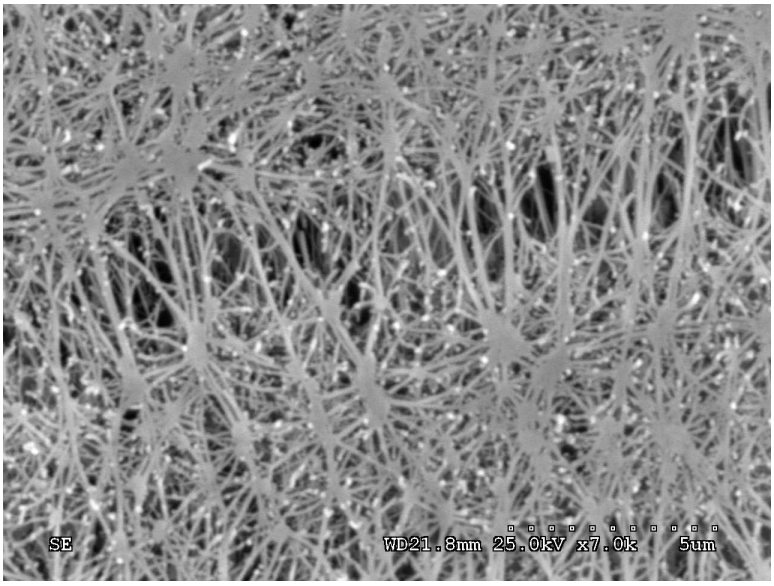

Figure 3.18. Close-up SEM image of PTFE microporous membrane.

From the SEM image, Fig. 3.17, we can see that it consists of multiple interlacing layers where the micropores almost uniformly distributed. As seen in the close-up SEM image, Fig. 3.18, the detailed microporous structure is noticed. At the same time, the length of the pores can be estimated. The rough length of micropores is about 15μm-30μm.

3.2.4 Experimental Setup and Results with a Straight Microchannel

A potassium hydroxide aqueous solution mixed with a m-cresol purple indicator was used as the solvent for investigating gas transfer efficiency through the PTFE microporous membrane. The measured average pH value of potassium hydroxide was 13. The aqueous solvent with indicator appeared purple. The purpose of using an indicator along with the reacting flow was to monitor the reaction progress by means of the pH color change. The indicator m-cresol purple can have a color change from purple to orange/yellow corresponding to a pH range of 7.6-9.2 in a basic solution. Regarding the aforementioned reaction kinetics in the previous section, it indicates a pH value drop because the final product is not strong base. In this study, two different concentrations of KOH (0.1M and 0.25M) will be used. With pH indicator detection technique, the color change distances were measured along with the reacting flow.

The volume of the gas channel is 0.017ml. The self-diffusion coefficient of CO_2 is 16mm^2/s. The diffusion length is the height of the channel which is 250 μm. The diffusion time can be calculated using Eqn. 3.27.

$$t_D = \frac{\lambda^2}{D} \tag{3.27}$$

The diffusion time of CO_2 is approximately 0.0039s. The residence time of CO_2 is calculated from Eqn. 3.28

$$t_R = \frac{V}{Q} \tag{3.28}$$

The residence time varied with the volume flow rate. Volume flow rate varied from 0.1 ml/hr to 1ml/hr and the corresponding residence time decreased from 612s to 61.2s. The residence time was much larger than the diffusion time, that was a desired factor in mass transfer system.

3.2.5 Numerical Model for Microreactor with a Straight Microchannel

At first, we started with straight channel flow with a length of 13.6 cm. A schematic image of the straight microchannel and a complete microreactor set-up are shown in Fig. 3.19. The schematic diagram of the flow element is shown in Fig. 3.20. To test the performance of the microporous membrane for gas absorption, we connected CO_2 and the solvent with the membrane microreactor. The flow rate of CO_2 is controlled by a rotameter, and the solvent solution is pumped through a syringe pump which also controls solution flow rate. The compressed high purity CO_2 is fed into the top channel and the KOH solution is pumped into the bottom channel. From the previous experiment, it clearly shows the relation between the solvent flow rate and the mass transfer efficiency.

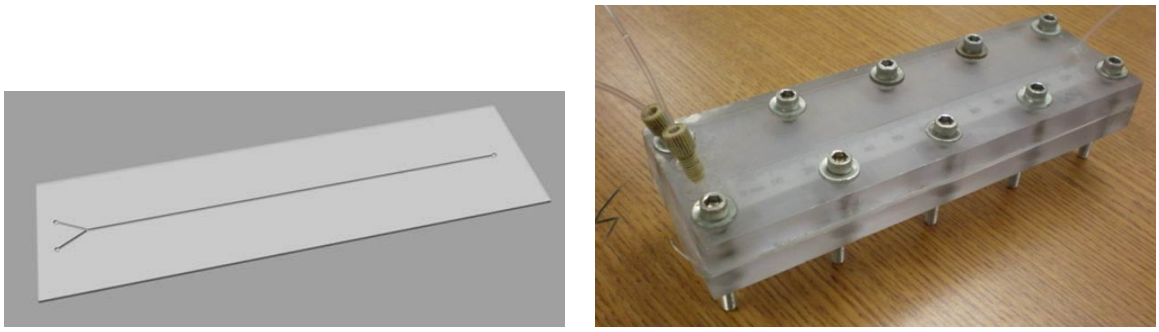

(a) (b)

Figure 3.19. PTFE membrane microreactor with a straight microchannel; (a) Y-shape microchannel, (b) a complete microreactor set-up.

Figure 3.20. Schematics of gas transport in the membrane microreactor.

To discover the influence of solvent flow rate on mass transfer performance, we fixed the gas flow rate and changed the solvent flow rate from 0.1mL/hr to 1mL/hr. At each flow rate, the location where solution color changed form purple to orange/yellow was marked. We collected the product from the liquid outlet and measured the pH value which was in a range of 8-8.5. It shows agreement with the reaction kinetics study aforesaid. For this test, we used two different concentrations of solvent, 0.1M and 0.25M. In the following figures, Fig. 3.21 and Fig. 3.22, they clearly show the color change zone along with the reacting flow. By testing different flow rates, the influence of solvent concentration on the transfer rate, can be seen in Fig. 3.23. The lower concentration of the solvent, the faster the reaction takes place when the gas was fed at same flow rate.

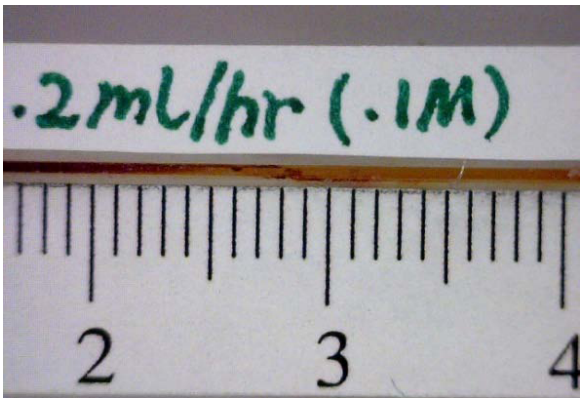

Figure 3.21. Color change zone for KOH concentration 0.1M.

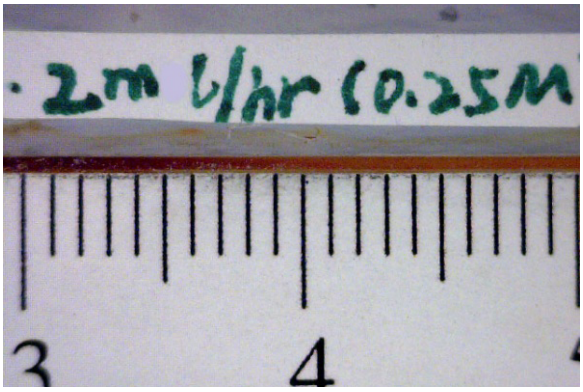

Figure 3.22. Color change zone for KOH concentration 0.25M.

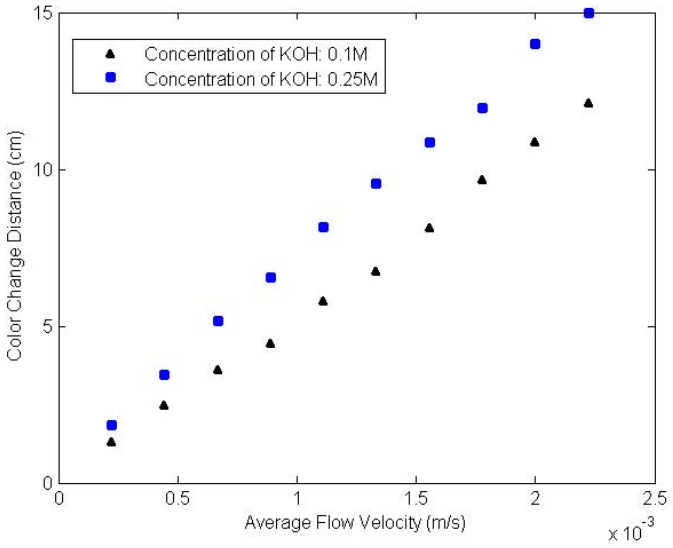

Figure 3.23. Color change distance comparison between different solvent concentration.

As seen in Fig. 3.21 and Fig. 3.22, the pH color change seems more thoroughly with lower concentration at same solvent flow rate than higher concentration. With a lower concentration, the pH color change zone is smaller than higher solvent concentration. However, the pH color change for higher concentration is stretching further to the downstream, that results in a longer reacting zone. It indicates that higher residence time is needed for higher concentration solvent, the is clearly shown in Fig. 3.23.

Mass transport for each species with chemical reactions is governed by continuity equation 3.29, momentum equation 3.30, and mass transport equation 3.31, which consists of a diffusion term, convection term, and reaction term.

$$\nabla \cdot \vec{v} = 0 \tag{3.29}$$

$$\rho(\vec{v} \cdot \nabla)\vec{v} = -\nabla p + \mu \nabla^2 \cdot \vec{v} \tag{3.30}$$

$$\frac{\partial C_i}{\partial t} = D_i \nabla^2 C_i - \vec{v} \cdot \nabla C_i + R_i \tag{3.31}$$

C_i, D_i, R_i are the concentration, diffusion coefficient, and reaction rate for each species, respectively. The reaction kinetics term R_i for each species was described in the previous section. The resistance to gas transport are from liquid phase, gas phase, and membrane itself. However, in a short review on gas transport given by Mansourizadeh and Ismail [30], it indicated that the resistance to gas transport from gas phase is negligible. In this case, microporous membrane was modeled as a wall with a constant mass fraction. Therefore, to simplify the computational model, only the liquid phase where the reaction took place was modeled. A two-dimensional rectangular domain was used. A structured mesh containing 200,000 elements was created using Pointwise V16, which is commercially available mesh generation software. A segment of microchannel with mesh is shown in Fig. 3.24. A boundary layer resolved mesh was constructed to capture the high concentration gradient near the microchannel wall and the membrane.

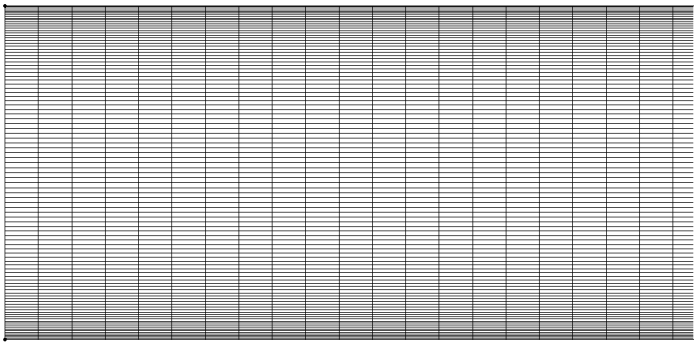

Figure 3.24. Structured mesh.

An incompressible steady state flow coupled with mass transport was solved by using the commercial solver Fluent. Appropriate boundary conditions were applied to solve the continuity equation, momentum equation, and mass transport equation, listed as Eqn. 3.29, Eqn 3.30, and Eqn. 3.31. For solving the flow field, a non-slip boundary condition was applied at the wall and the membrane. At the inlet, the average velocity, $\overline{v}$, of the solvent/pH indicator mixture was used. The outflow boundary condition was used at the outlet for an unknown pressure and velocity field. For solving the mass transport equation, the local mass fraction,Y_i, seen in Eqn. (3.32) for each species was defined as

$$Y_i = \frac{C_i M_{w,i}}{\rho_i} \tag{3.32}$$

Where, C_i (mol/L) is molar concentration, ρ_i (kg/m^3) is density, and $M_{w,i}$ (g/mol) is molecular weight. The index i represents A, B, C, and D, corresponding to KOH, CO_2, K_2CO_3, and $KHCO_3$, respectively. At the inlet, Y_A=1, Y_B=Y_C=Y_D=0. At the wall, the diffusion mass flux $\vec{J}_i$ (kg/m^2s) Eqn. 3.33 was set to 0 for all species.

$$\vec{J}_i = -D_i \nabla C_i \tag{3.33}$$

A liquid-gas interface at the bottom of the microchannel was modeled as the membrane. Henry's law was applied at the membrane, seen in Eqn. 3.34, which describes the ratio of the concentration of absorbed species in liquid at the interface to the concentration in the gas phase [62]. Henry's law constant, H, for CO_2 to aqueous system at 297 K is 0.8314 [63]. Since the mass flow rate of carbon dioxide was fixed and the flow was incompressible, the density was treated as a constant, which allowed a constant mass fraction of carbon dioxide to be applied to the membrane. For other

species, a zero diffusion mass flux was applied to the membrane to ensure no species cross the membrane.

$$C_{B,l} = HC_{B,g} \tag{3.34}$$

In Eqn. 3.34, l and g represent liquid phase and gas phase, respectively. B represents CO_2.

A steady state solution was obtained by using an implicit pseudo-time marching scheme. To investigate the influence of the flow velocity on the mass transport, five different volume flow rates, 0.1, 0.2, 0.3, 0.4, and 0.5 mL/hr, corresponding to the average flow velocities 2.22e-4 m/s, 4.44e-4 m/s, 6.66e-4 m/s, 8.88e-4 m/s, and 1.11e-3 m/s, were used in this study. In the following figure Fig. reffig:4contour, the mass fraction distribution of each species are presented at an average flow velocity of 2.22e-4 m/s. The physical and chemical properties of each species are listed in Table 3.5.

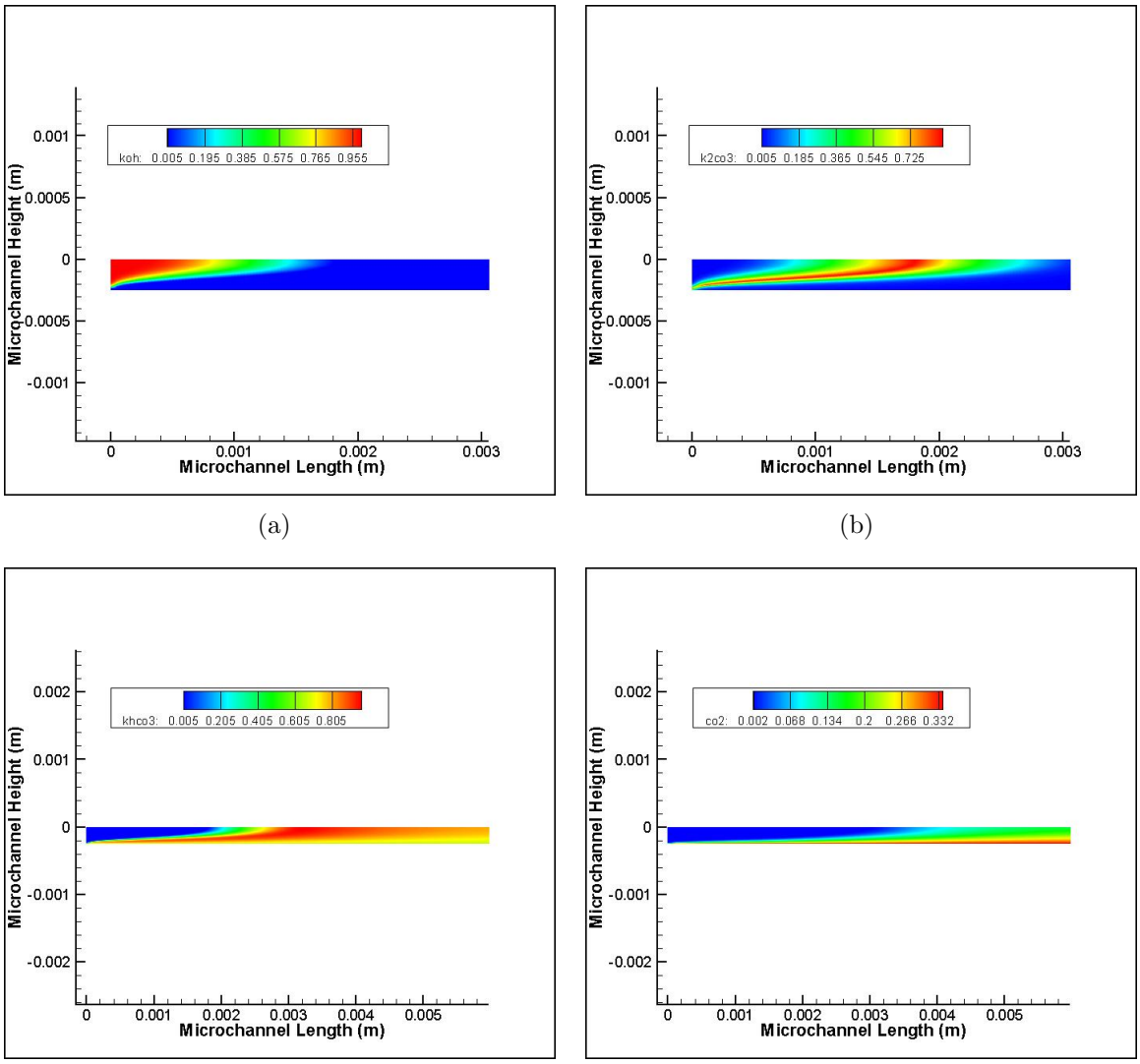

Figure 3.25. Mass fraction distribution of each species with an average flow velocity of 2.22e-4 m/s; (a) mass fraction distribution of KOH, (b) mass fraction distribution of K_2CO_3, (c) mass fraction distribution of $KHCO_3$, (d) mass fraction distribution of CO_2.

Table 3.5. Physical and chemical properties of each species at 297K 1atm

Speices	Molecular Weight (g/mol)	Densigy (kg/m^3)	Dynamic Viscosity ($Pa{\cdot}s$)
KOH	56.1	998	1e-3
CO_2	44	1.7878	1.4e-5
K_2CO_3	138.2	1264.7	1e-3
$KHCO_3$	100.1	1048	1e-3
H_2O	18	1000	1e-3

The steady state solution for different average flow velocities were obtained. The average mass fraction of each species vs. iteration number is shown in Fig. 3.26.

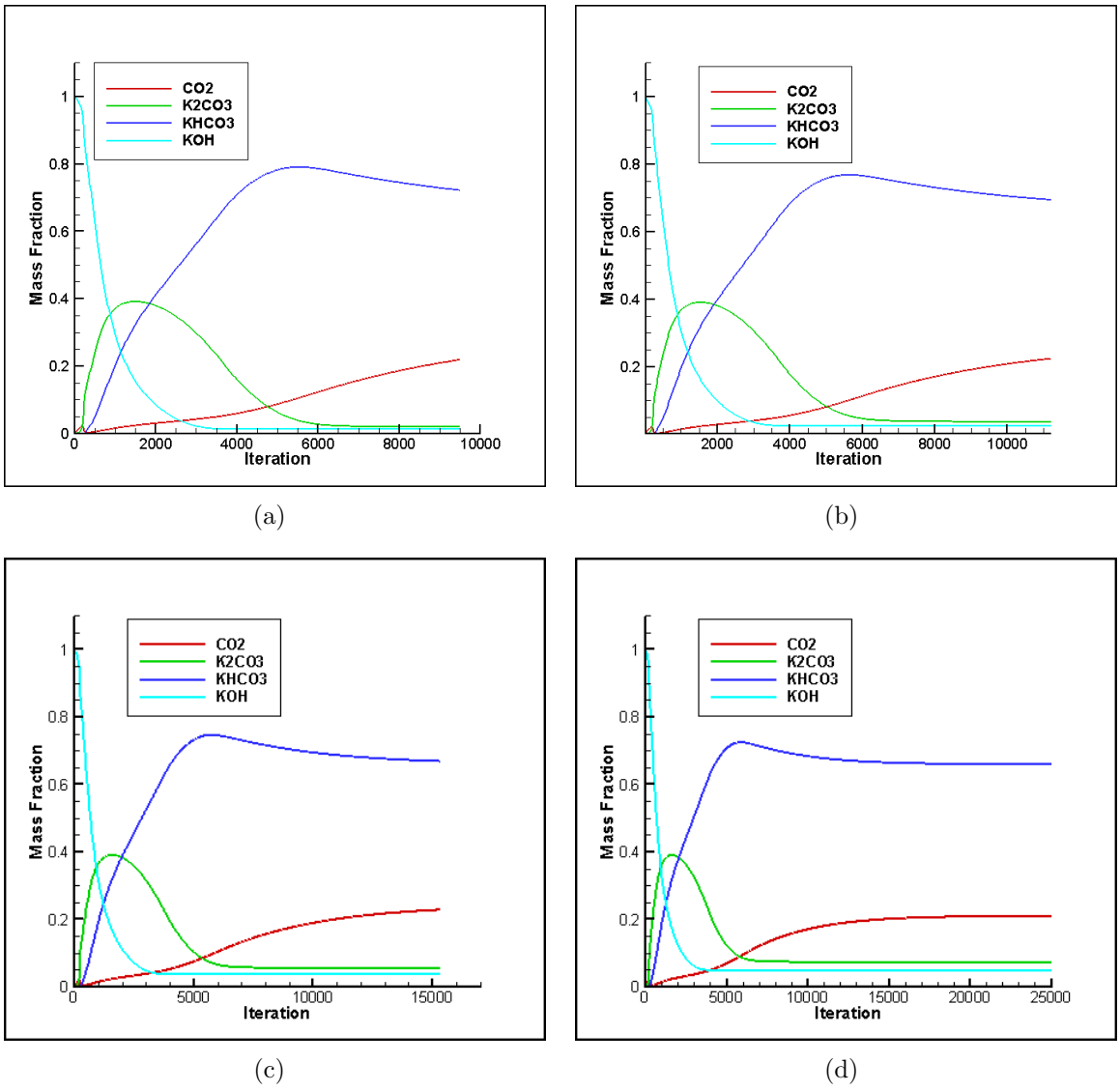

Figure 3.26. Average mass fraction of each species vs. iteration at (a) $\overline{v}$=2.22e-4 m/s, (b) $\overline{v}$=4.44e-4 m/s, (c) $\overline{v}$=6.66e-4 m/s, and (d) $\overline{v}$=8.88e-4 m/s.

From Fig. 3.26, it is found out that converged solution is obtained faster with a lower flow velocity than a higher flow velocity. Meanwhile, detailed reaction kinetics are also demonstrated at different average flow velocities in this study. Mass fraction of K_2CO_3 rapidly increases with decrease of KOH. Along with increase in mass fraction of CO_2, production of $KHCO_3$ occurs, and that becomes the last controlling

reaction. It indicates that reaction of Eqn. 3.7 is really shifting to the forward reaction, and the reaction is mainly dominated by the forward reaction until it reaches an equilibrium-state.

In the experiment, the pH color change location was spotted at location of the complete reaction. From the simulation results, the average mass fraction variation of $KHCO_3$ along the wall for different flow velocities is shown in Fig. 3.27. As expected, the reaction completion location varies with the average flow velocity. The location of completed reaction moves further downstream when the reacting flow at a higher flow velocity.

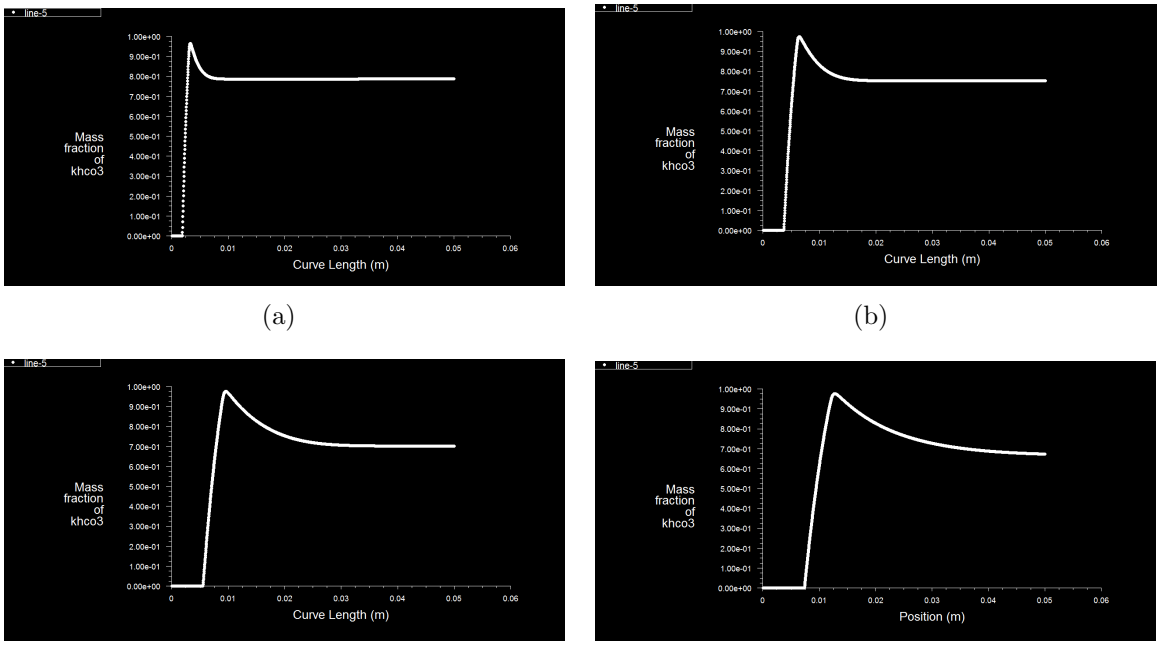

Figure 3.27. Average mass fraction variation of $KHCO_3$ along the wall at (a) $\overline{v}$=2.22e-4 m/s, (b) $\overline{v}$=4.44e-4 m/s, (c) $\overline{v}$=6.66e-4 m/s, and (d) $\overline{v}$=8.88e-4 m/s.

Production of $KHCO_3$ is not an instantaneous reaction. It is not only effected by the convection effect from flow field, but is also effected by the reaction kinetics

and molecular diffusion. In the following plot, Fig. 3.28, mass fraction distribution is stretching in downstream. Since the third controlling reaction Eqn. 3.7 is a reversible reaction, production of $KHCO_3$ is elongated even further downstream; meanwhile, along with the backward reaction, mass fraction of $KHCO_3$ is reducing until the equilibrium state is reached in the further downstream. The same phenomenon was also observed during the experiment.

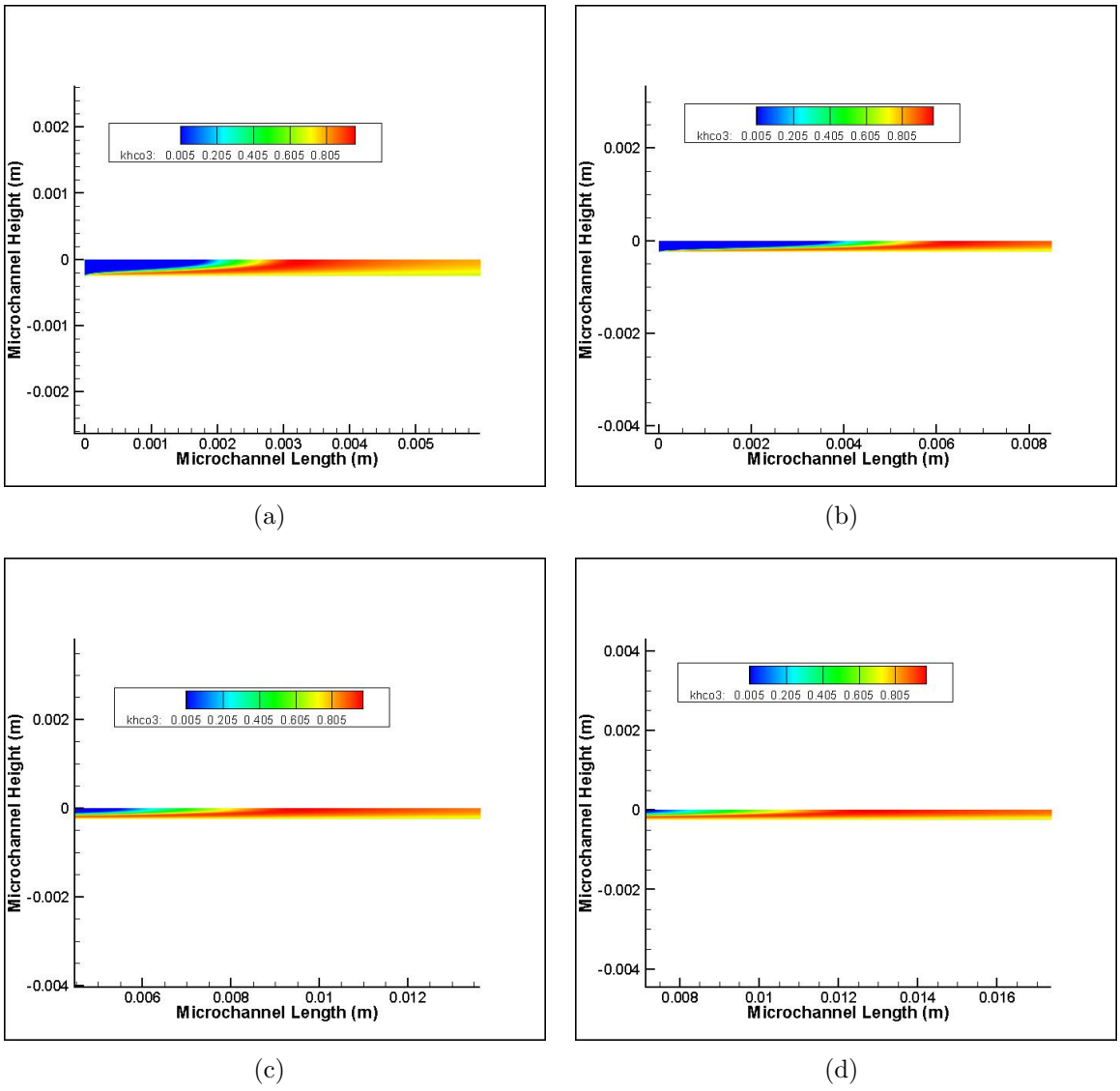

Figure 3.28. Mass fraction distribution of $KHCO_3$ at (a) $\overline{v}$=2.22e-4 m/s, (b) $\overline{v}$=4.44e-4 m/s, (c) $\overline{v}$=6.66e-4 m/s, and (d) $\overline{v}$=8.88e-4 m/s.

From the experiment results, it was noticed that the solvent concentrations also play an important role to the gas absorption efficiency. In simulation model, reactant ratio α was defined as the ratio of initial mass fraction of KOH to the constant mass fraction of CO_2 at the membrane. The removal efficiency η was also defined as the ratio between the absorbed mass fraction of CO_2 to the initial mass fraction of CO_2.

$$\eta = \frac{Y_{Absorbed,CO_2}}{Y_{Initial,CO_2}} \times 100\% \tag{3.35}$$

From the Henry's law, a constant mass fraction of 0.34 CO_2 was calculated using a concentration of 0.04M. Two reactant ratios, 1.47 and 2.94, were applied to calculate the removal efficiency with a constant average flow velocity of 4.44×10^{-4}m/s. With a reactant ratio 1.47, a removal efficiency of 53.17% was obtained; a removal efficiency of 65.93% was calculated by applying a reactant ratio of 2.94. The solvent concentration has significant effect on the removal efficiency. The higher concentration results in a higher removal efficiency. However, to obtain a better mixing with a higher concentration solvent, the longer residence time is needed. The second experiment was designed and carried with a new microchannel design. It has longer flow path in the same given area as the straight microchannel.

3.2.6 Experiment Setup and Results with a Meandering Microchannel

From the previous experiment, it was found that the flow rate is limited by the the residence time. With a request of higher flow rate, the longer residence time is desired. Based on the previous experimental results and observations, a meandering microchannel pattern was designed and fabricated. The schematic image is shown in Fig. 3.29. The complete reactor set-up is shown in Fig. 3.30.

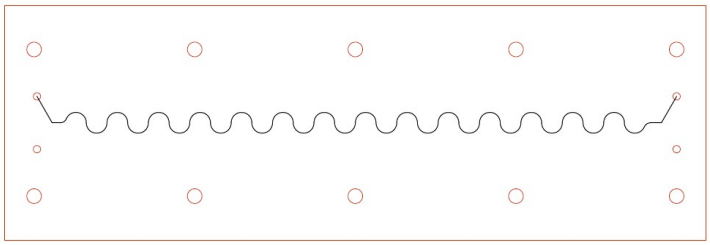

Figure 3.29. A schematic image of the meandering microchannel.

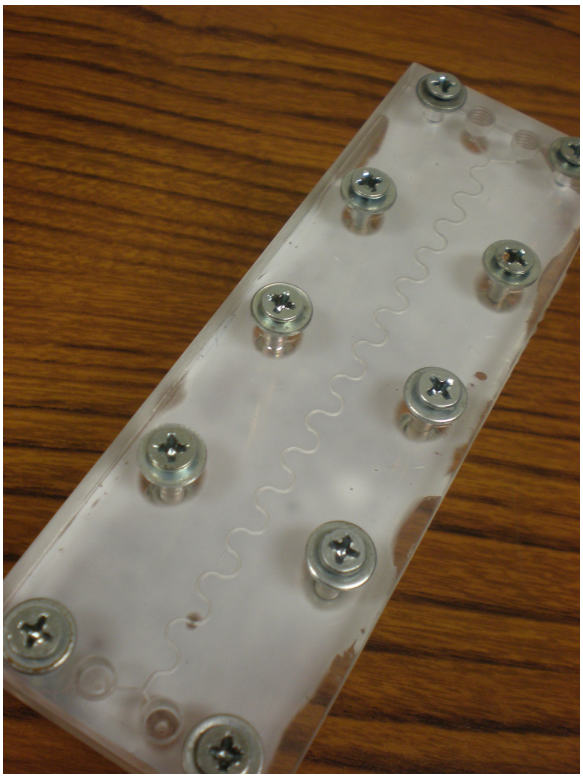

Figure 3.30. Meandering microchannel reactor set-up.

The fixture is same size as the one for the straight microchannel, however, the effective mixing length of the meandering channel is 43% longer than the straight microchannel on same given area. The advantage to have longer mixing zone is to engage longer residence time for high flow rate. The microchannel width is same as the straight micaochannel, 500μm; the mean radius of each curve is 2.25mm. The pH value of the solvent/indicator mixture is 12.96 for concentrations of 0.1M and 0.25M. The solution at outlet was collected and the pH value was measured. The average pH value is 8.18 after gas absorption using 0.1M KOH, while the average pH value is about 8.68 after gas absorption using 0.25M KOH.

Similar to the previous experiment apparatus and procedure, two different concentrations were used, 0.1M and 0.25M. The same pH indicator detection technique

was used to monitor the reaction progression. Two images were taken while the experiment was running, shown in Fig. 3.31 and Fig. 3.32. They clearly show the pH color changing zone along the channel. In this experiment, different gas volume flow rates was used to investigate the influence of gas flow rate on mass transport phenomenon. The gas flow rate was controlled by a rotameter; the rotameter was calibrated using a digital mass flow controller. Four different gas flow rates was used, 0.4606mL/min, 1.7084 mL/min, 5.0239 mL/min, and 12.4949 mL/min, variations of the pH color change with different flow velocities are shown in Fig. 3.33 and Fig. 3.34. They both show a linear relation between the pH color change distance and the average flow velocity. Both cases showed that insignificant influence of the gas flow rate on gas transport cross the PTFE microporous membrane.

Figure 3.31. The pH color change along the meandering microchannel.

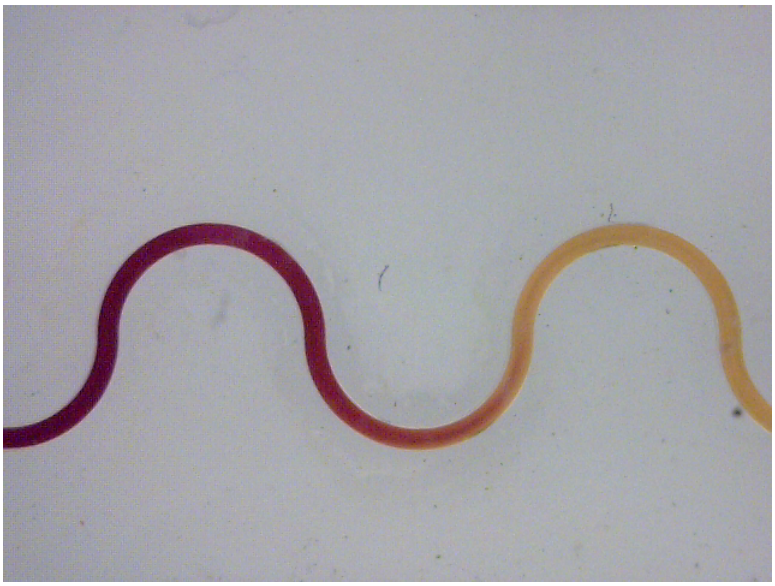

Figure 3.32. A close-up view of pH color change zone.

As seen in Fig. 3.31, the obvious pH color change from upstream to downstream is observed. In the downstream, pH color stays in a light yellow which indicates a complete conversion of CO_2. In a close-up view of the pH color change zone, it shows a clear image of pH color change along the reacting flow in a small segment of meandering microchannel. The pH color transition along the microchannel indicates that mass transfer within liquid phase is not only dominated by reaction kinetics rate but is also effected by flow field.

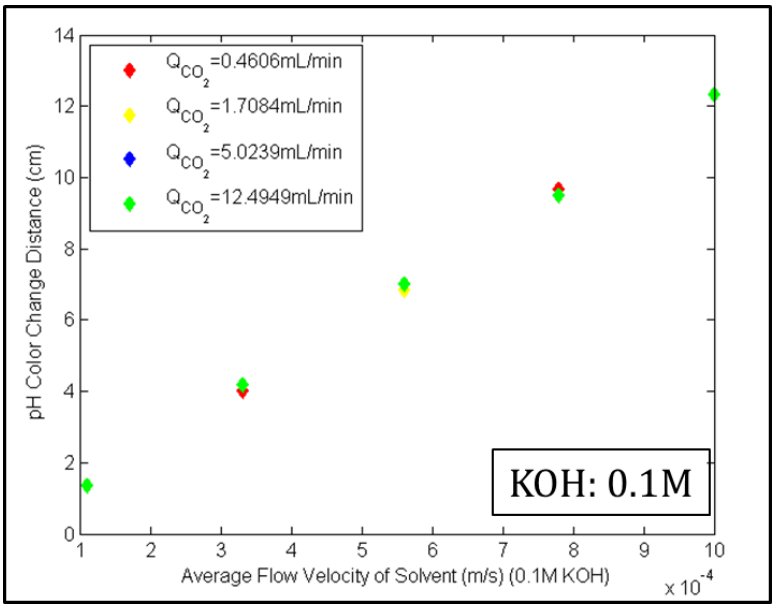

Figure 3.33. pH color change distance with different average flow velocities for a solvent concentration of 0.1M.

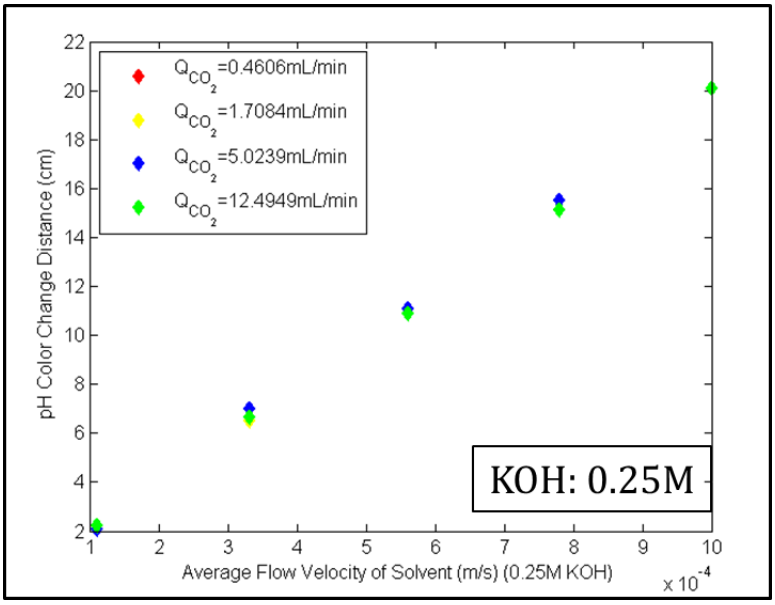

Figure 3.34. pH color change distance with different average flow velocities for a solvent concentration of 0.25M.

From these two cases, it clearly shows a linear relation between liquid flow rate and pH color change distance along the microchannel. Same as performance was observed as previous study with a straight microchannel. Longer residence time was required with higher solvent concentration. Compared to straight microchannel, a complete CO_2 conversion was was able to obtained with higher flow velocity. In addition, smaller pH color change zone is observed in a meandering channel indicates that the effect of convection in mass transfer is stronger than molecular diffusion. on the other hand, the Results obtained from the simulation also indicate the proportional relationship between the distance and solvent flow rate. By testing different microchannel patterns, it is found that the meandering microchannel allows for a higher flow rate in the liquid phase, which helps the channel pattern design to meet high flow rate requirement. The second test demonstrated the insignificant effect of gas flow rate on gas absorption along the reacting flow. It also indicated that gas absorption rate depends on the concentration of the solvent, since reaction kinetics play a very important role in the gas absorption process. From the results of the simulation, the distribution of each species along with the reacting flow were predicted.

3.2.7 Numerical Model for Microreactor with a Meandering Microchannel

A three-dimensional model was established for the meandering microchannel. In this model, a partial meandering microchannel was modeled. The entrance and the exit were modeled as straight duct to enable the fully developed flow condition. The hexahedral element was used to construct the mesh for the computational domain in Pointwise, mesh plot is seen in Fig. 3.35.

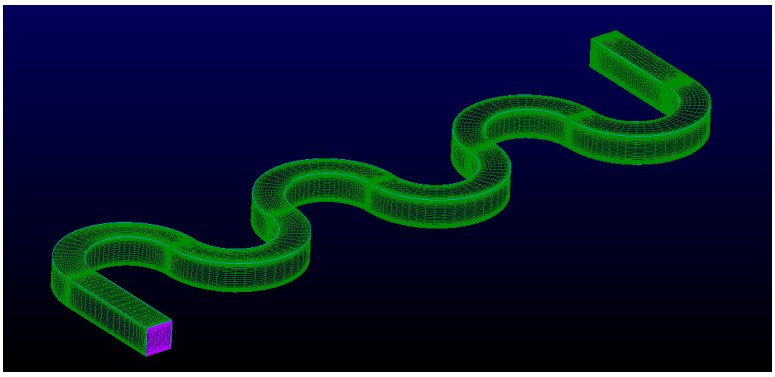

Figure 3.35. Structured mesh with 422,000 hexahedral elements.

Similar to the straight microchannel set up, the computational model for meandering microchannel was also established for the liquid phase. The top surface was treated as the channel upper wall, and the bottom of channel was assigned as the membrane. A set of three-dimensional governing equations Eqn. 3.29, Eqn. 3.30, and 3.31 were solved using a commercial CFD solver Fluent. A steady state solution with an average velocity of 2.22×10^{-4} was obtained. The mass fraction distribution of each species is shown in the following figures Fig. 3.36.

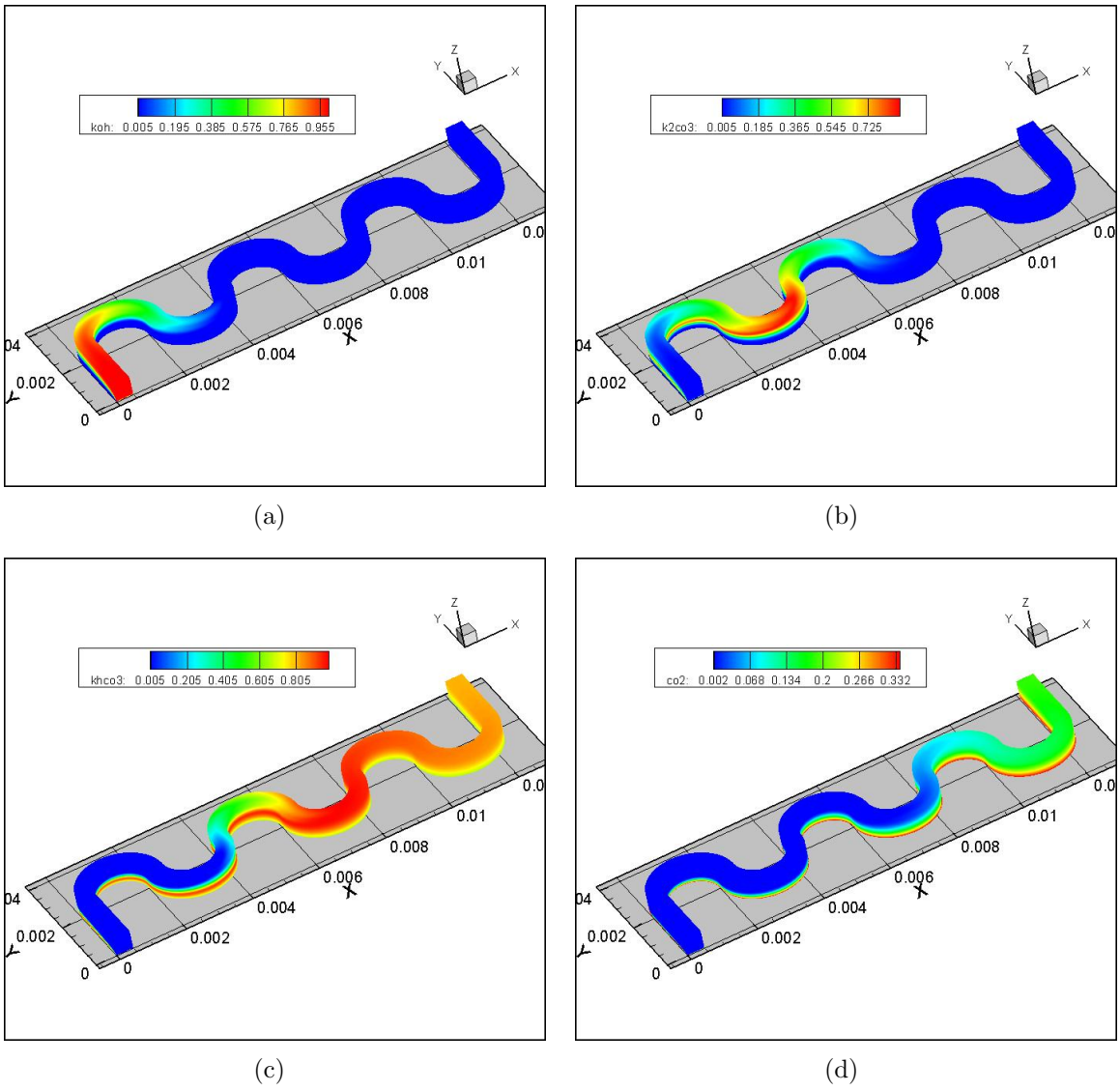

(a) (b)

(c) (d)

Figure 3.36. Mass fraction distribution of each species with an average flow velocity of 2.22e-4 m/s; (a) mass fraction distribution of KOH, (b) mass fraction distribution of K_2CO_3, (c) mass fraction distribution of $KHCO_3$, (d) mass fraction distribution of CO_2.

The results showed the clear reaction kinetics and the mass fraction distribution of each species in a three-dimensional meandering microchannel. Along with the decrease in KOH, the production of the K_2CO_3 was increased rapidly with fast

reaction rate. At the same time, the mass fraction of CO_2 in the liquid phase was increasing along the reacting flow, which resulted in the production of $KHCO_3$ along the flow. With a small reaction rate, the production of $KHCO_3$ was stretching further to the downstream. With the mass fraction increase of CO_2 into the liquid phase, the forward reaction of Eqn. 3.7 was much stronger than the back reaction due to the excessive of CO_2. In addition, the CO_2 diffusion path is predicted along the microchannel and shown in a 3D contour plot. As shown in Fig. 3.36(d), mass fraction of CO_2 is increasing along with reacting flow, and it reaches highest value when production of $KHCO_3$ starts. However, with strong forward reaction of Eqn. 3.7, CO_2 is decreasing to produce $KHCO_3$ until reaction reaches equilibrium state.

CHAPTER 4

CONCLUSIONS AND DISCUSSIONS

4.1 Conclusions and Discussions

In the present work, two major types of microreactors have been studied, including the design, fabrication, testing, and numerical validation. First, a microreactor was designed with liquid-liquid slug flow for immiscible fluids mixing. A simple neutralization reaction was used to demonstrate the mass transfer. We came up with a simple and efficient way to quantify the mass transfer performance using pH indicator detection technique. Results show the significant effect of flow rate on the mixing and slug size controlling. Mass transfer in liquid-liquid slug flow is not only dominated by molecular diffusion but also effected by convection. In addition, the rate constant of the applied chemical reaction was found by using experimental data and an optimization algorithm. The investigation of mass transfer using two-phase slug flow in a capillary microreactor has been presented at the 2010 COMSOL conference in Boston, MA. The computational results biodiesel production in a capillary microreactor simulation were published and presented at the 2011 ASME IDETC/CIE conference.

Another microreactor we designed was a gas-liquid membrane microreactor. A compact PTFE microprous membrane reactor was designed, built, and tested. The performance of the PTFE membrane has been demonstrated. The experiments were carried out for two different gases, oxygen and carbon dioxide. Two different gases were used to investigate mass transfer in gas-liquid system. They were all studied with a chemical reaction involved. In terms of a pH value change throughout the chemical

reaction, the same pH indicator detection technique was used to monitor reaction progression along the reacting flow. A hydrophobic microporous membrane was used in this study, that significantly reduced the resistance for gas transfer through membrane. However, it found out that partial wetting occurred for the chemical reaction with catalyst involved. The catalyst might be retained on the membrane, that might cause micropores partially blocked. Therefore, the solubility of the catalyst and the concentration of dissolved catalyst should be carefully adjusted. Additionally, the Sherwood numbers were presented for two cases and demonstrated a significant convective effect on gas transport through the microporous membrane. An approximate linear relationship between Reynolds number and Sherwood number was observed for two study cases. By comparing with a literature data, it indicates that smaller characteristic length improves the mixing efficiency in a gas-liquid system.

The gas transport testing through a PTFE microporous membrane was extended to a prototype gas absorption microreactor design. An alkaline aqueous solution was chosen as the solvent. The detailed reaction kinetics were presented in this study. With assistance of a pH indicator detection technique, we were able to examine the effects of the gas flow rate and liquid flow rate on gas transfer into an aqueous solvent. Two different channel pattern were presented. Experimental study and numerical study were both conducted for two designs. The significant effect of sloven flow velocity was observed in the experiment and predicted with a 2D computational model. The two dimensional computer simulation was established to predict detailed reaction kinetics and gas transport phenomena. Throughout this study, two different solvent concentration were used. For a higher solvent concentration, longer residence time required and a longer pH color change zone was observed. It shows that the mass transfer with a chemical reaction involved is not only dominated by convection but is also dominated by the reaction rate.

To study with a higher flow rate, a meandering microchannel was design based on the same given area as the straight microchannel. As expected, the meandering microchannel was able to handle higher flow rate than the straight microchannel. Meanwhile, a more thorough pH color change was observed along reacting flow in the meandering microchannel. A three dimensional model was built using a small microchannel segment. Results from simulation draw the conclusion as the results from the experiment and reaction mechanism study. The completion of reaction in this reacting flow is not only effected by reaction kinetics, but is also effected by the flow rate in a continuous reacting flow. In this study, different gas flow rate was used in the gas transport experiment, and it shows an insignificant effect of gas flow rate on the gas transport to the aqueous solvent. It is concluded that major resistance to mass transfer in gas-liquid system was from the liquid side. In addition, by using two different solvent concentration, simulation results predict that the higher concentration gives better CO_2 conversion with a longer residence time in the meandering microchannel. In a gas-liquid system, the solvent concentration, solvent flow rate, characteristic length, and membrane selection are the major factors to be considered for enhancing gas absorption efficiency.

4.2 Recommended Future Work

To the simulation model for gas absorption, the characteristics of membrane could be added, such as porosity, thickness, and permeability. The two phase could be constructed for gas absorption study. To the experiment, the flow rate and concentration of absorbed gas at exit could be measured for calculating the liquid side mass transfer coefficient, gas side mass transfer coefficient, and overall mass transfer coefficient.

REFERENCES

[1] N. Kockmann, O. Brand, G. K. Fedder, C. Hierold, J. G. Korvink, and O. Tabata, *Advanced Micro Nanosystems: Fundamentals, Devices, Fabrication, and Applications*. Weinheim, Germany: WILEY-VCH Verlag GmbH Co. KGaA, 2006.

[2] M. Matlosz, W. Ehrfeld, and J. Baselt, *Microreaction Technology, IMRET 5: Proceedings of the Fifth International Conference on Microreaction Technology*. Germany: Springer-Verlag Berlin Heidelberg, 2001.

[3] W. Ehrfeld, V. Hessel, and H. Löwe, *Microreactor: New Technology for Modern Chemistry*. Weinheim, Germany: Wiley-VCH Verlag GmbH, 2000.

[4] L. Cavin, A. Renken, and L. Kiwi-Minsder, "Liquid-liquid two-phase flow patterns and mass transfer characteristics in rectangular glass microreactors," *Chemical Engineering Science*, vol. 63, pp. 4035–4044, 2008.

[5] Y. Okubo, T. Maki, N. Aoki, T. Khoo, Y. Ohmukai, and K. Mae, "Liquid-liquid extraction for efficient synthesis an separation by utilizing micro spaces," *Chemical Engineering Science*, vol. 63, pp. 4070–4077, 2008.

[6] Y. Okubo, T. Maki, F. Nakanishi, T. Hayashi, and K. Mae, "Precise control of polymer particle properties using droplets in the microchannel," *Chemical Engineering Science*, vol. 65, pp. 386–391, 2010.

[7] F. Jiang, K. Drese, S. Hardt, M. Küpper, and F. Schönfeld, "Helical flows and chaotic mixing in curved micro channels," *AlChE*, vol. 50, pp. 2297–2305, 2004.

[8] S. Nagrath, L. Sequist, S. Maheswaran, D. Bell, D. Irimia, L. Ulkus, M. Smith, E. Kwak, S. Digumarthy, A. Muzikansky, P. Ryan, U. Balis, R. Tompkins,

D. Haber, and M. Toner, "Isolation of rare circulating tumour cells in cancer patients by microchip technology," *Nature*, vol. 450, pp. 1235–1239, 2007.

[9] Y. Lim, A. Kouzani, and W. Duan, "Lab-on-a-chip: A component view," *Microsystem Technologies*, vol. 16, pp. 1995–2015, 2010.

[10] S. Lu, "Nanoporous and nanostructured material for catalysis, sensor, and gas separation applications," *Journal of Nanomaterials*, vol. 2006, pp. 1–2, 2006.

[11] R. Svitek and W. Federspiel, "A mathematical model to predict CO_2 removal in hollow fiber membrane oxygenator," *Annals of Biomedical Engineering*, vol. 36, pp. 992–1003, 2008.

[12] N. Loney, "Analytical solution to mass transfer in laminar flow in hollow fiber with heterogeneous chemical reaction," *Chemical Engineering Science*, vol. 51, pp. 3995–3999, 1996.

[13] S. Eslami, S. Mousavi, S. Danesh, and H. Banazadeh, "Modeling and simulation of CO_2 removal from power plant flue gas by pg solution in a hollow fiber membrane contactor," *Advances in Engineering Software*, vol. 42, pp. 612–620, 2011.

[14] M. Kashid, D. Agar, and S. Turek, "Cfd modelling of mass transfer with and without chemical reaction in the liquid-liquid slug flow microrector," *Chemical Engineering Science*, vol. 62, pp. 5102–5109, 2007.

[15] X. Wang, H. Hirano, and N. Okamoto, "Numerical investigation on the liquid-liquid, two phase flow in a y-shaped microchannel," *ANZIAM J.*, vol. 48, pp. C963–C976, 2008.

[16] A. Soleymani, E. Kolehmainen, and I. Turunen, "Numerical and experimental investigations of liquid mixing in t-type micromixers," *Chemical Engineering Journal*, vol. 135S, pp. S219–S228, 2008.

[17] Y. Zhao, G. Chen, and Q. Yuan, "Liquid-liquid two-phase mass transfer in the t-junction microchannels," *ALChE Journal*, vol. 53, pp. 3042–3053, 2007.

[18] J. Burns and C. Ramshaw, "The intensification of rapid reactions in multiphase systems using slug flow in capillaries," *Lab on A Chip*, vol. 1, pp. 10–15, 2001.

[19] M. Kashid and D. Agar, "Hydrodynamics of liquid-liquid slug flow capillary microreactor: Flow regimes, slug size and pressure drop," *Chemical Engineering Journal*, vol. 131, pp. 1–13, 2007.

[20] H. Löwe and W. Ehrfeld, "State-of-the-art in microreaction technology: Concepts, manufacturing and application," *Electrochimica Acta*, vol. 44, pp. 3679–3689, 1999.

[21] A. Manz and H. Becker, *Microsystem Technology in Chemistry and Life Sciences*. Germany: Springer-Verlag Berlin Heidelberg, 1998.

[22] J. Sun, J. Ju, L. Ji, L. Zhang, and N. Xu, "Synthesis of biodiesel in capillary microreactors," *Ind. Eng. Chem. Res.*, vol. 47, pp. 1398–1403, 2008.

[23] A. Bhattacharya, "General kinetic model for liquid-liquid phase-transfer-catalyzed reactions," *Ind. Eng. Chem. Res.*, vol. 35, pp. 645–652, 1996.

[24] Y. Zhao, G. Chen, and Q. Yuan, "Liquid-liquid two-phase flow patterns in a rectangular microchannel," *AIChE Journal*, vol. 52, pp. 4052–4060, 2006.

[25] M. Rhee and M. A. Burns, "Drop mixing in a microchannel for lab-on-a-chip platforms," *Langmuir*, vol. 24, pp. 590–601, 2008.

[26] M. Kashid, D. F. Rivas, D. Agar, and S. Turek, "On the hydrodynamics of liquid-liquid slug flow capillary microreactors," *Asia-Pac. J. Chem. Eng.*, vol. 3, pp. 151–160, 2008.

[27] B. Logan, *Environmental Transport Processes*. New York: Wiley, John Sons, 1999.

[28] R. Brodkey and H. Hershey, *Transport Phenomena: A Unified Approach.* Singapore: McGraw-Hill Inc., 1988.

[29] R. Reid, J. Prausnitz, and T. Sherwood, *The Properties of Gases and Liquids, 3d ed.* New York: McGraw-Hill, 1977.

[30] A. Mansourizadeh and A. Ismail, "Hollow fiber gas-liquid membrane contactors for acid gas capture: A review," *Journal of Hazardous Materials*, vol. 171, pp. 38–53, 2009.

[31] K. Esato and B. Eiseman, "Experimental evaluation of Gore-Tex membrane oxygenator," *J. Thorac. Cardiovas. Surg.*, vol. 68, pp. 690–697, 1975.

[32] T. Tsuji, K. Suma, K. Tanishita, H. Fukazawa, M. Kanno, H. Hasegawa, and A. Takahashi, "Development and clinical evaluation of hollow fiber membrane oxygenator," *Transactions-American Society for Artificial Internal Organs*, vol. 27, pp. 280–284, 1981.

[33] Z. Qi and E. Cussler, "Microporous hollow fibers for gas absorption. II. Mass transfer across the membrane," *J. Membr. Sci.*, vol. 23, pp. 333–345, 1985.

[34] Y. Lee, R. Noble, B. Yeom, Y. Park, and K. Lee, "Analysis of CO_2 removal by hollow fiber membrane contactors," *Journal of Membrane Science*, vol. 194, pp. 57–67, 2001.

[35] V. Dindore and G. Versteeg, "Gas-liquid mass transfer in a cross-flow hollow fiber module: Analytical model and experimental validation," *International Journal of Heat and Mass Transfer*, vol. 48, pp. 3352–3362, 2005.

[36] A. Marjani and S. Shirazian, "CFD simulation of SO_2 removal from gas mixtures using ceramic membranes," *World Academy of Science, Engineering and Technology*, vol. 58, pp. 868–871, 2011.

[37] X. Zhang, W. Zhang, X. Hao, H. Zhang, Z. Zhang, and J. Zhang, "Mathematical model of gas permeation through ptfe porous membrane and the effect of membrane," *Chinese J. Chem. Eng.*, vol. 11, pp. 383–387, 2003.

[38] J. Zou, J. Huang, and W. W. Ho, "CO_2 water gas shift membrane reactor for fuel cell hydrogen processing," *Ind. Eng. Chem. Res.*, vol. 46, pp. 2272–2279, 2007.

[39] C. Park and D. Kim, "Dual-channel microreactor for gas-liquid syntheses," *J. AM. CHEM. SOC.*, vol. 132, pp. 10 102–10 106, 2010.

[40] J. Franco, S. Kentish, J. Perera, and G. Stevens, "Poly(tetrafluoroethylene) sputtered polypropylene membranes for carbon dioxide separation in membrane gas absorption," *Ind. Eng. Chem. Res.*, vol. 50, pp. 4011–4020, 2011.

[41] E. Drioli, E. Curcio, and G. Profio, "State of the art and recent progresses in membrane contactors," *Chem. Eng. Res. Des.*, vol. 83, pp. 223–233, 2005.

[42] Z. Qi and E. Cussler, "Microporous hollow fibers for gas absorption. I. Mass transfer in the liquid," *J. Membr. Sci.*, vol. 23, pp. 321–332, 1985.

[43] E. Nagy, *Basic Equations of the Mass Transport through a Membrane Layer*. 225 Wyman Street, Waltham, MA 02451, USA: Elsevier Inc., 2012.

[44] P. Keshavarz, J. Fathikalajahi, and S. Ayatollahi, "Mathematical modelling of the simultaneous absorption of carbon dioxide and hydrogen sulfide in a hollow fiber membrane contactor," *Separation and Purification Technology*, vol. 63, pp. 145–155, 2008.

[45] P. Feron and A. Jansen, "Capture of carbon dioxide using membrane gas absorption and reuse in the horticultural industry," *Energy Convers. Mgml*, vol. 36, pp. 411–414, 1995.

[46] G. Agrahari, N. Verma, and P. Bhattacharya, "Application of hollow fiber membrane contactor for the removal of carbon dioxide from water under liquid-liquid extraction mode," *Journal of Membrane Science*, vol. 375, pp. 323–333, 2011.

[47] S. Iversen, V. Bhatia, K. Dam-Johansen, and G. Jonsson, "Characterization of microporous membranes for use in membrane contactors," *J. Membr. Sci.*, vol. 130, pp. 205–217, 1997.

[48] P. Dunlap and S. Faris, "Surface tension of aqueous solutions of potassium hydroxide," *NATURE*, vol. 196, pp. 1312–1313, 1962.

[49] S. Wickramasinghe, J. Garcia, and B. Han, "Mass and momentum transfer in hollow fibre blood oxygenators," *Journal of Membrane Science*, vol. 208, pp. 247–256, 2002.

[50] A. Goerke, J. Leung, and S. Wickramasinghe, "Mass and momentum transfer in blood oxygenators," *Chemical Engineering Science*, vol. 57, pp. 2035–2046, 2002.

[51] R. Dugas and G. Rochelle, "CO_2 absorption rate into concentrated aqueous monoethanolamine and piperazine," *Journal of Chemical Engineering Data*, vol. 56, pp. 2187–2195, 2011.

[52] M. Jassim, G. Rochelle, D. Eimer, and C. Ramshaw, "Carbon dioxide absorption and desorption in aqueous monoethanolamine solutions in a rotating packed bed," *Ind. Eng. Chem. Res.*, vol. 46, pp. 2823–2833, 2007.

[53] V. Dindore, D. Brilman, and G. Versteeg, "Modelling of cross-flow membrane contactors:Mass transfer with chemical reaction," *Journal of Membrane Science*, vol. 255, pp. 275–289, 2005.

[54] H. Hikita, S. Asai, and T. Takatsuka, "Absorption of carbon dioxide into aqueous sodium hydroxide and sodium carbonate-bicarbonate solutions," *The Chemical Engineering Journal*, vol. 11, pp. 131–141, 1976.

[55] A. Cents, D. Brilman, and G. Versteeg, "CO_2 absorption in carbonate/bicarbonate solutions: The Danckwerts-criterion revisited," *Chemical Engineering Science*, vol. 60, pp. 5830–5835, 2005.

[56] R. V. Bhat, J. Kuipers, and G. Versteeg, "Mass transfer with complex chemical reactions in gas-liquid systems: two-step reversible reactions with unit stoichiometric and kinetic orders," *Chemical Engineering Journal*, vol. 76, pp. 127–152, 2000.

[57] C. Tsonopolous, D. Coulson, and L. Inman, "Ionization constants of water pollutants," *J. Chem. Eng. Data*, vol. 21, pp. 190–193, 1976.

[58] M. Sharma and P. Danckwerts, "The absorption of carbon dioxide into solutions of alkalis and amines (with some notes on hydro gen sulphide and carbonyl sulphide)," *Chem. Eng.*, pp. CE245–CE280, 1966.

[59] D. Roberts and P. Danckwerts, "Kinetics of CO_2 in alkaline solution-I," *Chem. Eng. Sci.*, vol. 17, pp. 967–969, 1967.

[60] X. Wang, W. Conway, R. Burns, N. McCann, and M. Maeder, "Comprehensive study of the hydration and dehydration reaction of carbon dioxide in aqueous solution," *J. Phys. Chem. A*, vol. 114, pp. 1734–1740, 2010.

[61] G. Astarita, "Absorption of carbon dioxide into alkaline solutions in packed towers," *I EC Fundamentals*, vol. 2, pp. 294–297, 1963.

[62] S. Karoor and K. Sirkar, "Gas absorption studies in microporous hollow fiber membrane modules," *Ind. Eng. Chem. Res.*, vol. 32, pp. 674–684, 1993.

[63] J. Geankoplis, *Mass Transport Phenomena*. Columbus, OH: Ohio State University Bookstores, 1972.

BIOGRAPHICAL STATEMENT

Wei Han received her Bachelor of Science degree from Xi'an Polytechnic University, Shaanxi, China in 2006 and her Ph.D degree in Mechanical Engineering from The University of Texas at Arlington in 2012. She is a student member of ASME and SWE. Her current research interests include experimental and numerical investigation of mass transfer in microreactors and microfluidic device design. This includes manufacturing and testing, as well as computational simulation using the Finite Element Method and CFD techniques.